

Aerofoil tones at moderate Reynolds number

Christopher K. W. Tam[†] and Hongbin Ju

Department of Mathematics, Florida State University, Tallahassee, FL 32306-4510, USA

(Received 15 October 2010; revised 17 September 2011; accepted 18 October 2011;
first published online 1 December 2011)

It is known experimentally that an aerofoil immersed in a uniform stream at a moderate Reynolds number emits tones. However, there have been major differences in the experimental observations in the past. Some experiments reported the observation of multiple tones, with strong evidence that these tones are most probably generated by a feedback loop. There is also an experiment reporting the observation of a single tone with no tonal jump or other features associated with feedback. In spite of the obvious differences in the experimental observations published in the literature, it is noted that all the dominant tone frequencies measured in all the investigations are in agreement with an empirically derived Paterson formula. The objective of the present study is to perform a direct numerical simulation (DNS) of the flow and acoustic phenomenon to investigate the tone generation mechanism. When comparing with experimental studies, numerical simulations appear to have two important advantages. The first is that there is no background wind tunnel noise in numerical simulation. This avoids the signal-to-noise ratio problem inherent in wind tunnel experiments. In other words, it is possible to study tones emitted by a truly isolated aerofoil computationally. The second advantage is that DNS produces a full set of space–time data, which can be very useful in determining the tone generation processes. The present effort concentrates on the tones emitted by three NACA0012 aerofoils with a slightly rounded trailing edge but with different trailing edge thickness at zero degree angle of attack. At zero degree angle of attack, in the Reynolds number range of 2×10^5 to 5×10^5 , the boundary layer flow is attached nearly all the way to the trailing edge of the aerofoil. Unlike an aerofoil at an angle of attack, there is no separation bubble, no open flow separation. All the flow separation features tend to increase the complexity of the tone generation processes. The present goal is limited to finding the basic tone generation mechanism in the simplest flow configuration. Our DNS results show that, for the flow configuration under study, the aerofoil emits only a single tone. This is true for all three aerofoils over the entire Reynolds number range of the present study. In the literature, it is known that Kelvin–Helmholtz instabilities of free shear layers generally have a much higher spatial growth rate than that of the Tollmien–Schlichting boundary layer instabilities. A near-wake non-parallel flow instability analysis is performed. It is found that the tone frequencies are the same as the most amplified Kelvin–Helmholtz instability at the location where the wake has a minimum half-width. This suggests that near-wake instability is the energy source of aerofoil tones. However, flow instabilities at low subsonic Mach numbers generally do not cause strong tones. An investigation of how near-wake instability generates tones is carried out using the space–time data provided by numerical simulations. Our observations indicate that the dominant tone generation process is the interaction of the oscillatory motion of the near wake, driven by flow instability, with the trailing edge

[†] Email address for correspondence: tam@math.fsu.edu

of the aerofoil. Secondary mechanisms involving unsteady near-wake motion and the formation of discrete vortices in regions further downstream are also observed.

Key words: aeroacoustics

1. Introduction

Small wind turbines are generally operated at moderate Reynolds numbers. It is known experimentally that an aerofoil with profiles designed for wind turbine application in the Reynolds number range of 5×10^4 to 6×10^5 generates distinct tones (see Oerlemans 2003). The first systematic study of aerofoil tones was carried out by Paterson *et al.* (1973). Since this pioneering work, there have been many experimental investigations of the aerofoil tone phenomenon. Surprisingly, there are significant differences in the experimental results. Furthermore, there is no clear consensus on the tone generation mechanism even to this day.

Paterson *et al.* (1973) performed their aerofoil tone experiment in an open wind tunnel using primarily a NASA0012 aerofoil. Figure 1 is one of their principal results. In this figure the tone frequencies are plotted against the flow velocity. One of the salient features of this set of data is the ladder-like structure. The data points in figure 1 are from measurements at 4–10 degrees angle of attack. But they also reported that tones were observed even at zero degree angle of attack and for a NACA0018 aerofoil. Because the ladder-like structure is formed by data at different angles of attack, it appears that the tone frequency versus flow velocity pattern is somewhat insensitive to the angle of attack. The ladder-like structure was soon recognized by Tam (1974) as an indication that the observed tones were related to a feedback loop. Based on the data of Paterson *et al.* (1973), Tam found that the data pattern at 6° angle of attack fitted the formula

$$f = 6.85nU^{0.8}, \quad (1.1)$$

where f is the tone frequency in hertz, U is the flow velocity in feet per second and n is an integer. A feedback loop must satisfy an integral-wavenumber constraint. The different steps of the ladder structure are a consequence of a change in the quantization number n of (1.1). An increase in n by one corresponds to an increase of one wave in the loop and the move to the next step in figure 1. At certain flow velocities, two tones were measured simultaneously, e.g. at AB of figure 1. If the velocity increases slightly beyond the velocity at A, the dominant tone frequency jumps to the next ladder step as indicated by A to B. This is usually referred to as staging. Further increase in velocity causes the subdominant tone to vanish. By analysing their data carefully, Paterson *et al.* (1973) found that the dominant frequency followed a $U^{1.5}$ power law, as indicated by the full line in figure 1. Based on their extensive measurements, they proposed the following formula for the dominant tone frequency, f :

$$f = \frac{0.011U^{1.5}}{(C\nu)^{1/2}}, \quad (1.2)$$

where C is the chord width and ν is the kinematic viscosity. Equation (1.2) has since been referred to as the Paterson formula. As a part of their investigation, Paterson

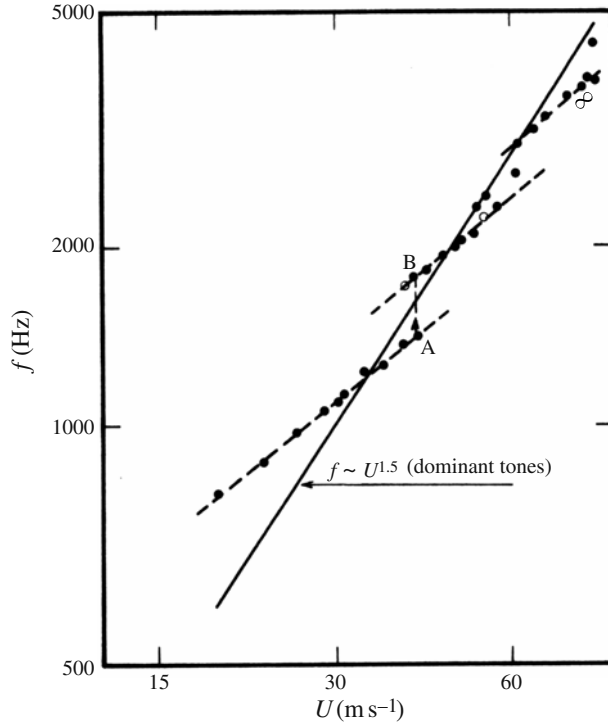


FIGURE 1. Relationship between tone frequency and flow velocity for NACA0012 aerofoils measured by Paterson *et al.* (1973). The full line is the Paterson formula.

et al. (1973) measured spanwise surface pressure correlations on the aerofoil. They found strong spanwise correlation over a considerable extent of the aerofoil surface. Specifically, they reported a normalized cross-correlation of nearly unity for spanwise separation distance of one chord width (the model in the experiment is only slightly longer than two chord widths in the spanwise direction). This indicates that the flow phenomenon associated with aerofoil tones is quite two-dimensional.

Arbey & Bataille (1983) repeated the open wind tunnel aerofoil experiment. They performed all their NACA0012 measurements at zero degree angle of attack. They did not observe discrete tones as Paterson *et al.* (1973). What they observed were tones superimposed on a broadband spectrum. In fact, there is a multitude of tones; as many as 12 were measured. Figure 2 shows a typical spectrum of their measurements. Arbey & Bataille discovered that the frequency of the dominant tone (f_s in the centre of the spectrum of figure 2) was in good agreement with the Paterson formula, (1.2). Figure 3 shows a replot of their dominant tone data as Strouhal number versus Reynolds number. The straight line in figure 3 is the Paterson formula. Other than the agreement in the dominant tone frequencies, the other results of the two experiments are quite different. First of all, Arbey & Bataille measured many tones but Paterson *et al.* had, at most, two tones simultaneously. Moreover, the frequencies of the two tones in the Paterson *et al.* experiment are separated by a magnitude of about five times that of the tones of Arbey & Bataille. When the full set of data are plotted in the frequency versus velocity diagram, the tones of Arbey & Bataille also form a ladder-like structure, suggesting again that the tones are related to a feedback loop.

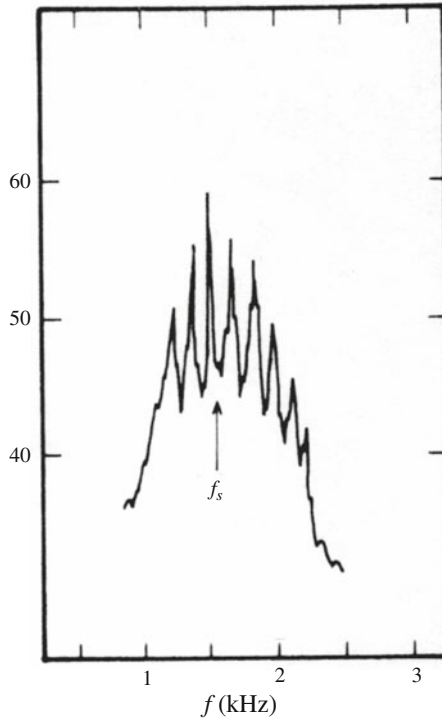


FIGURE 2. Spectrum of aerofoil tones measured by Arbey & Bataille (1983).

Unlike Paterson *et al.* (1973) and Arbey & Bataille (1983), Nash, Lowson & McAlpine (1999) performed their aerofoil experiment inside a wind tunnel. They quickly realized that the cross-duct modes and the Parker modes of the wind tunnel could interfere with the aerofoil tone phenomenon. To eliminate this possibility, they lined the wind tunnel walls with sound-absorbing materials. Under such an experimental condition, they found for each free stream velocity that there was a single aerofoil tone and no ladder structure. They suggested that the ladder-like structure data of Paterson *et al.* and Arbey & Bataille were influenced by their experimental facilities. The feedback and ladder-like data structure were not characteristics of the aerofoil tone phenomenon. The feedback loop apparently was locked on something in the experimental facility outside the open wind tunnel. However, at low angle of attack, the tone frequency versus flow velocity relation measured by Nash *et al.* is also in good agreement with the Paterson formula (see figure 4). At higher angle of attack, 4° or more, because of the blockage of the wind tunnel by the model, the measured relationship deviates from the Paterson formula, as would be expected.

Recently, there have been a number of new aerofoil tone experiments (see e.g. Nakano, Fujisawa & Lee 2006; Kurotaki *et al.* 2008; Chong & Joseph 2009). The experiment of Nakano *et al.* did not use the NACA0012 aerofoil. Thus their data are not suitable for comparison with the previously mentioned experiments. The paper by Kurotaki *et al.* is primarily a report of their numerical simulation work. However, the paper does mention briefly the results of an aerofoil tone experiment. The data are replotted in figure 5. It is clear from this figure that there are multiple tones. The tones have a ladder-like structure pattern. The pattern resembles the Parker and cross-duct

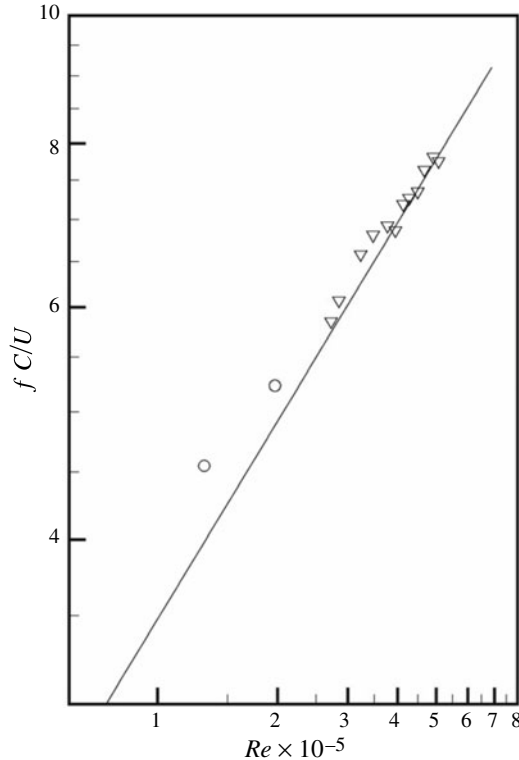


FIGURE 3. Relationship between the Strouhal number of the dominant tones and the Reynolds number measured by Arbey & Bataille (1983). The straight line is the Paterson formula.

mode observed in the initial experiment (without the installation of sound-absorbing acoustic liners) of Nash *et al.* (1999). The straight line in this figure is the Paterson formula. It correlates well with the dominant tone frequencies over a range of flow velocities.

It should be clear at this time that there are significant disagreements among the many aerofoil experiments we have been able to find in the literature. One major issue is whether the basic tone generation mechanism is related to a feedback loop, which would generate multiple tones, or whether, as in the observation by Nash *et al.* (1999), feedback is spurious and there should only be a single tone. Even among investigators who have observed multiple feedback tones, the details of the observed phenomenon are quite different. Therefore, it is fair to say that, at this time, no two experiments have the same results. On the other hand, regardless of the major differences, almost all experiments seem to agree that the Paterson formula yields a good prediction of the dominant tone frequencies. This is true over a wide range of Reynolds number.

What is the mechanism responsible for the generation of aerofoil tones? Beginning with the work of Paterson *et al.* (1973), a number of possible tone generation mechanisms have been proposed. Paterson *et al.* envisioned that they were vortex shedding tones similar to those associated with blunt trailing edges. Earlier, Sharland (1964) had made a similar suggestion. Tam (1974), Fink (1975) and Arbey & Bataille (1983) proposed that the source of energy responsible for aerofoil tones was the Tollmien–Schlichting instabilities in the boundary layer of the aerofoil. Nash *et al.*

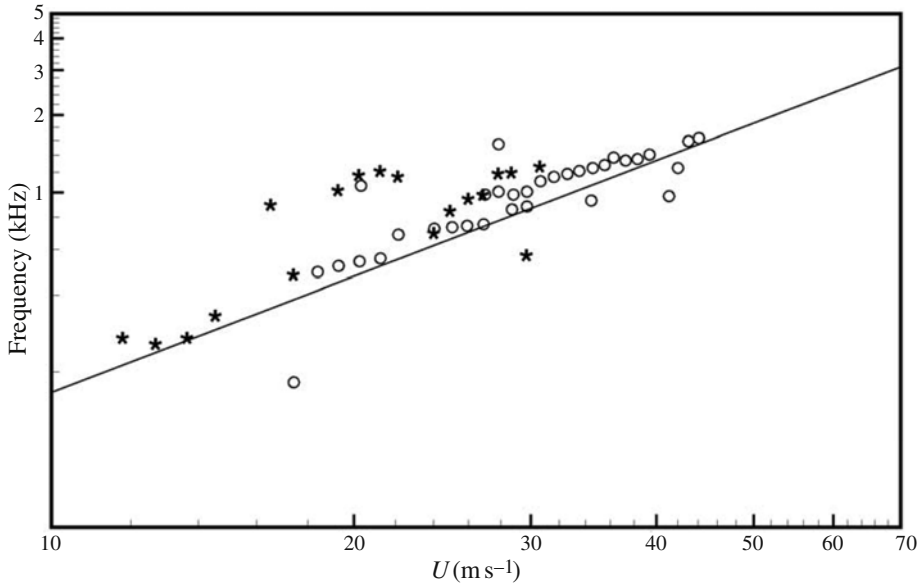


FIGURE 4. Relationship between aerofoil tone frequency and flow velocity measured by Nash *et al.* (1999): stars, 2° angle of attack; circles, 3° angle of attack; straight line, Paterson formula.

(1999) and later McAlpine, Nash & Lowson (1999) made detailed computations of the total growth of Tollmien–Schlichting instability waves in the boundary layer of NACA0012 aerofoils at an angle of attack. They found that the growth rate was small until the waves reached the separated flow region. They reported that the frequency of the instability wave with the highest total growth was very close to the tone frequency. The point of their effort is that the most amplified wave is responsible for causing tone generation. Recently, this idea was further pursued by Desquesnes, Terracol & Sagaut (2007), Sandberg, Sandham & Joseph (2007) and Kingan & Pearse (2009). It is worthwhile to mention that Lowson, Fides & Nash (1994) reported that they observed Tollmien–Schlichting waves in an aerofoil boundary layer at a lower Reynolds number than the first appearance of aerofoil tone. They cautioned that boundary layer instability is not a sufficient condition for aerofoil tone generation. On the other hand, Nash *et al.* (1999) reported the observation of separated flow on the aerofoil but without any tone. They concluded that flow separation is not a sufficient condition for tone generation.

Tam (1974) was the first to propose that the ladder-like structure of the data of Paterson *et al.* (1973) is because the tones were generated by a feedback loop. This idea was followed by Fink (1975) and expanded by Arbey & Bataille (1983) and recently by Jones & Sandberg (2010). If feedback is, indeed, a part of the tone generation mechanism for an isolated aerofoil, there would have to be a feedback point on the surface of the aerofoil. Arbey & Bataille proposed that the maximum-velocity point on the surface of the aerofoil is the feedback point. On the other hand, Fink and Jones & Sandberg appear to regard the aerofoil leading edge as the feedback point. Physically, the feedback point should be located where the flow is most receptive to external excitation. Unfortunately, in the absence of a receptivity analysis, it is not

In the second case, the angle of attack is 5° and the Reynolds number is 10^5 . Flow separation is observed in both cases. Desquesnes *et al.* performed locally parallel hydrodynamic stability analysis of the separated boundary layer. They found that the frequency of the most amplified instability wave was very close to the frequency of the strongest tone.

Kurotaki *et al.* (2008) carried out a large eddy simulation (LES) of the aerofoil tone phenomenon. An implicit LES approach was used. In their work, the approximate deconvolution method originally developed by Stolz, Adams & Kleiser (2001) for filtering out the high wave components of the solution was adopted. A C-type mesh was used to form a body-fitted grid around a NACA0015 aerofoil. In their study, the aerofoil is placed at 5° angle of attack. Three cases at Reynolds number of 4×10^5 , 6×10^5 and 8×10^5 are computed. The results are displayed in figure 5. In spite of the fact that it is a thicker aerofoil, the computed tone frequencies are in good agreement with the Paterson formula (see figure 5).

More recently, Sandberg *et al.* (2009) reported the results of their numerical simulations of aerofoil tones. They confined their work to a NACA0012 aerofoil at 0° , 5° and 7° angles of attack. The flow Mach number was 0.4 and the Reynolds number was 5×10^4 . No tone was found at 0° angle of attack. At 5° angle of attack, a separation bubble formed on the suction side of the aerofoil. At 7° angle of attack, open separation took place. As a follow-up to the work of Sandberg *et al.* (2009), Jones & Sandberg (2010) repeated a similar computation at a slightly higher Reynolds number of 10^5 . The angles of attack in this work were 0° , 0.5° , 1.0° and 2.0° . They performed instability wave analysis of the aerofoil boundary layer. They reported that the most amplified convectively unstable instability wave frequency was significantly higher than the measured tone frequency.

The primary objective of this study is to perform two-dimensional DNS of the aerofoil tone generation phenomenon using a specially designed body-fitted multi-size grid, a high-order, high-resolution computational scheme and a set of high-quality radiation and outflow boundary conditions. The use of two-dimensional simulations is justified, as the measured fluctuations in the Paterson *et al.* (1973) experiment displayed strong spanwise coherence. Also, in all the previous numerical studies of aerofoil tones cited above, the investigators are unanimously of the opinion that two-dimensional simulations are good and reasonable approximations. The present effort concentrates on the simulation of NACA0012 aerofoils with a slightly rounded trailing edge at zero degree angle of attack. The principal reason for restricting the study to zero degree angle of attack is to keep the flow configuration as simple as possible. At zero degree angle of attack, the boundary layer is attached nearly all the way to the trailing edge. There is no separation bubble, no large-scale open separation. This eliminates possible acoustic feedback sites on the surface of the aerofoil. Figure 6 shows our computed vorticity distribution in the boundary layer and the near wake of a NACA0012 aerofoil (2% truncation) at zero degree angle of attack. There is no vortex shedding at the trailing edge. The wake simply forms smoothly at the trailing edge by the merging of the boundary layers on the two sides of the aerofoil. The wake is unstable and rolls up into discrete vortices some distance downstream of the trailing edge of the aerofoil. This eliminates vortex shedding as a tone generation mechanism.

The first aim of our simulations is to see if aerofoil tone is a single tone or consists of multiple tones. Our second aim is to establish a computed relation between tone frequency and flow velocity. This relation is then used to match the Paterson formula. A good match not only will serve as a validation of the computational algorithm and code but also would assure that the simulation contains the essential physics of the

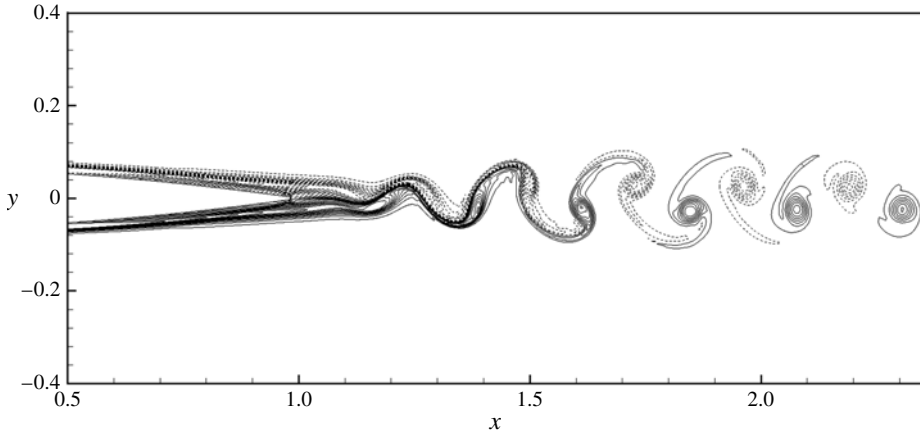


FIGURE 6. Computed instantaneous vorticity distribution in the boundary layer and the near wake of a NACA0012 aerofoil (2% truncation) at zero angle of attack. The Reynolds number is 2×10^5 .

tone generation mechanism. Once this is accomplished, our third goal is to use the computed space–time DNS data to investigate the energy source of the tones and the processes by which the tones are produced. It is useful to point out that there are intrinsic advantages in a DNS study. In comparison with experiments, there is no wind tunnel background noise to mask the aerofoil noise spectrum. Also by using high-quality computational aeroacoustics methods, there is less possibility of introducing a facility-associated feedback loop. The aerofoil under study can be made almost totally isolated. Therefore, by eliminating as many unwarranted sources of noise that could influence the generation of feedback tones as possible, it is our hope that the basic tone generation mechanism can be determined to a satisfactory level, although it is possible that other tone generation mechanisms could become important at non-zero degree angle of attack.

The rest of the paper is as follows. In §2, the computational model of the present study is described. The computational grid and computational algorithm used in all the simulations are also discussed. To ensure that our simulations have the needed resolution, we have performed grid refinement analysis. The details are provided at the end of this section. Section 3 reports the results of tone frequencies measured in our DNS study. Comparisons with the Paterson formula are made. Good agreements are found. Section 4 focuses on the energy source of aerofoil tones. We propose that it is the instabilities of the near-wake flow that drives the aerofoil tones. To support our proposition, a non-parallel aerofoil wake instability investigation has been performed. A tone frequency formula as a function of the flow velocity is established through the results of instability analysis. This formula is in good agreement with DNS tone frequency measurements. It is known that flow instabilities at low subsonic Mach number are not an efficient sound generator. For this reason, a study of the processes by which near-wake instability leads to tone generation is carried out. The results are reported in §5. Section 6 concludes and summarizes the main results of the present investigation.

2. Computational model, grid design, algorithm and grid refinement

This is a computational study of the generation of aerofoil tones. It is known that the quality of a numerical simulation depends critically on the quality and resolution

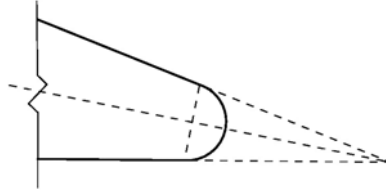


FIGURE 7. Blunt trailing edge aerofoil formed by adding a rounded edge to a truncated aerofoil.

Aerofoil	Truncation (%)	Width of chord (cm)	Trailing edge thickness (cm)
NACA0012	0	10	0
no. 1	0.5	9.956	0.014
no. 2	2.0	9.82	0.055
no. 3	10.0	9.1	0.248

TABLE 1. Aerofoil dimensions and thicknesses.

of the computational grid and the algorithm used. As the accuracy of our computed results and hence the conclusions of this investigation rely on our grid design and chosen computational algorithm, we will provide some of the important details below.

2.1. Computational model

We will consider only NACA0012 aerofoils at zero degree angle of attack, as in the experiment of Arbey & Bataille (1983). A secondary objective of the present study is to investigate the effect of blunt trailing edge on the frequencies of aerofoil tones. To make an aerofoil with blunt trailing edge, we first truncate the sharp trailing edge of an aerofoil at a prescribed percentage of chord. The truncated aerofoil is then fitted with a rounded trailing edge as shown in figure 7. Table 1 lists the dimensions of the three truncated aerofoils used in the present investigation. The trailing edge profiles of these three aerofoils are shown in figure 8. Here the aerofoil with 0.5% truncation is considered practically a sharp trailing edge aerofoil. Its tonal characteristics will be used to compare with the Paterson formula.

In this study, the original aerofoil chord width is 0.1 m. The aerofoil is placed in a uniform stream with a velocity U . The Reynolds number range of the present study is from 2×10^5 to 5×10^5 . The corresponding velocity range is 29–72.5 m s⁻¹. The Mach number range is 0.0853–0.213. For a flat plate with the same length, the displacement thickness at the trailing edge at a Reynolds number of 2×10^5 is $\delta^* = 1.72 (C\nu/U)^{1/2} = 3.85 \times 10^{-4}$ m. Thus, R_{δ^*} is equal to 770. For this Reynolds number, the wake flow is laminar in the absence of high-level ambient turbulence and sound. In the present numerical simulations, there is a total absence of free stream turbulence and sound waves (except for the aerofoil tone). As a result, the flow tends to remain laminar for Reynolds numbers that would be transitional experimentally. We find that, in our simulations, the boundary layer is laminar even at the highest Reynolds number of our study.

The governing equations are the dimensionless Navier–Stokes equations in two dimensions and the energy equation. Here the length scale is C (chord width), velocity scale is a_∞ (ambient sound speed), time scale is C/a_∞ , density scale is ρ_∞ (ambient

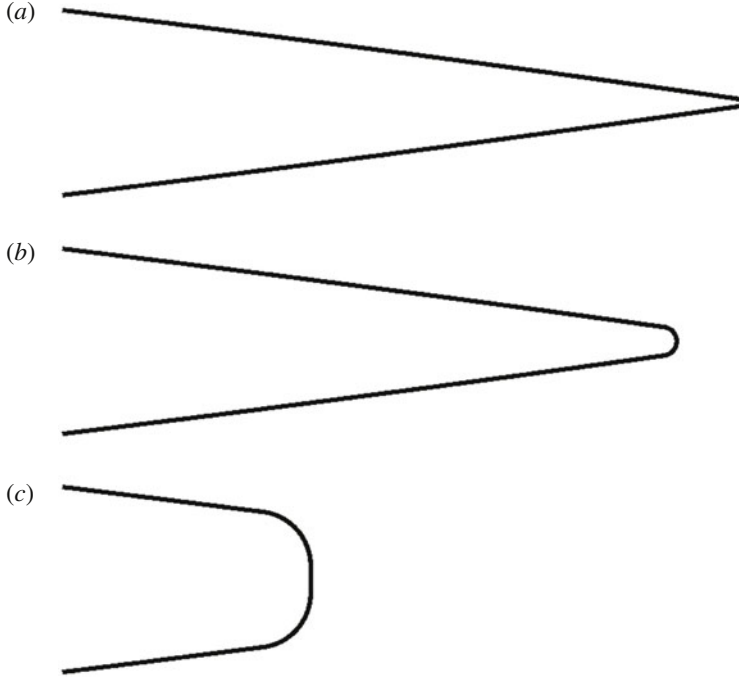


FIGURE 8. Trailing edge profiles of the three NACA0012 aerofoils used in the present study: (a) 0.5% truncation; (b) 2% truncation; (c) 10% truncation.

gas density), and pressure and stress scales are $\rho_\infty a_\infty^2$. These equations are

$$\frac{\partial \rho}{\partial t} + \rho \frac{\partial u_j}{\partial x_j} + u_j \frac{\partial \rho}{\partial x_j} = 0, \quad (2.1)$$

$$\frac{\partial u_i}{\partial t} + u_j \frac{\partial u_i}{\partial x_j} = -\frac{1}{\rho} \frac{\partial p}{\partial x_i} + \frac{1}{\rho} \frac{\partial \tau_{ij}}{\partial x_j}, \quad (2.2)$$

$$\frac{\partial p}{\partial t} + u_j \frac{\partial p}{\partial x_j} + \gamma p \frac{\partial u_j}{\partial x_j} = 0, \quad (2.3)$$

where

$$\tau_{ij} = \frac{M}{R_C} \left(\frac{\partial u_i}{\partial x_j} + \frac{\partial u_j}{\partial x_i} \right), \quad R_C = \frac{CU}{\nu}, \quad M = \frac{U}{a_\infty}. \quad (2.4)$$

U is the free stream velocity, M is the Mach number and R_C is the Reynolds number based on chord width. Both viscous dissipation and heat conduction are neglected in the energy equation, as the Mach number is small.

2.2. Computational grid

The first requirement of a quality numerical simulation is a well-designed grid. The grid exerts a significant control over the local and global resolution. For the aerofoil tone problem, a good resolution of the aerofoil surface boundary layer and the near wake is of paramount importance. This calls for a body-fitted grid with fine meshes adjacent to the aerofoil surface and in the wake region.

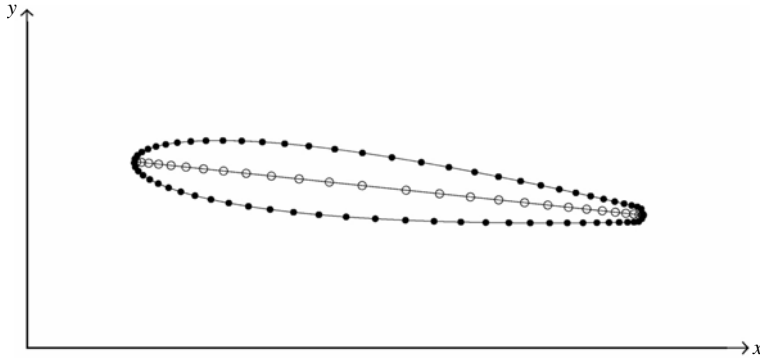


FIGURE 9. Source distribution along the camber line, and enforcement points on the aerofoil surface.



FIGURE 10. Mapping of the aerofoil into a slit in the w plane.

A popular grid design for aerofoil computation is the C -grid. But the C -grid can lead to singularity and non-smooth grid lines at the C -junction. To ensure that the grid used is of the highest quality, we use a specially designed grid generated by conformal mapping. The use of conformal mapping to generate a computational grid is not new. However, it has seldom been used for aerofoil configuration. For this reason, we believe it is worthwhile to elaborate on a few of the crucial steps in constructing the grid.

The method consists of two essential steps, as schematically illustrated in figures 9–11. The first step is a mapping of the aerofoil in the physical x - y plane into a slit in the w or the ξ - η plane. This is accomplished by conformal transformation using a multitude of point sources distributed along the camber line of the aerofoil, as shown in figure 9. The appropriate form of the conformal transformation is

$$w = z + \sum_{j=1}^N Q_j \log \left(\frac{z - z_j}{z - z_0} \right) + i\Omega, \tag{2.5}$$

where $w = \xi + i\eta$ represents the complex coordinates of a point in the mapped plane, $z = x + iy$ is a point in the physical plane, Q_j , z_j ($j = 1, 2, \dots, N$) are the source strengths and locations, and Ω is just a constant. The inclusion of Ω in the mapping function is important. Its inclusion makes it possible to map the aerofoil onto a slit on

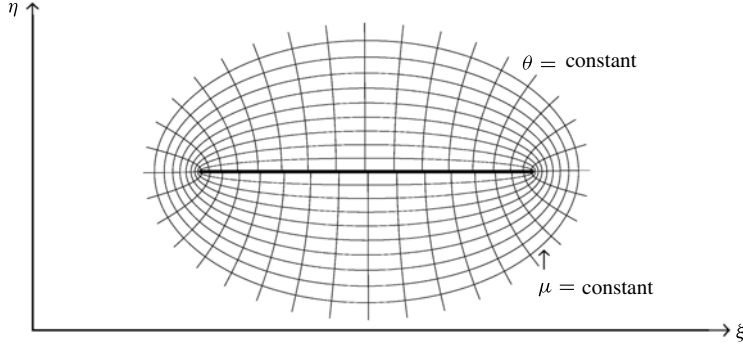


FIGURE 11. Elliptic coordinates around the slit as body-fitted grid for the aerofoil.

the real axis of the w plane (see figure 10). Finally, z_0 is the location of a reference source. A good location to place z_0 is in the middle of the camber line such that all the lines joining z_j to z_0 lie within the aerofoil. In this way, the branch cuts associated with the log functions of (2.5) would not present a problem in the computation.

In implementing the mapping, the coordinates z_j ($j = 1, 2, 3, \dots, N$) of the source points are first assigned. A useful rule in assigning the source locations is that the distance $|z_j - z_{j-1}|$ should be proportional in some way to the local thickness of the aerofoil. That is to say, the sources should be closer together where the aerofoil is thin. Now the source strengths Q_j ($j = 1, 2, \dots, N$) are to be chosen to accomplish the mapping. For this purpose, a set of points z_k ($k = 1, 2, \dots, M$) around the surface of the aerofoil are chosen to enforce the mapping; z_k are referred to as the enforcement points, and M should be much larger than N . Imposing the conditions that the surface of the aerofoil be mapped onto a slit on the real axis of the w plane on (2.5) leads to the following system of linear equations for Q_j and Ω :

$$y_k + \sum_{j=1}^N \text{Im} \left[Q_j \log \left(\frac{z_k - z_j}{z_k - z_0} \right) \right] + \Omega = 0, \quad k = 1, 2, \dots, M. \tag{2.6}$$

This system of equations may be written in matrix form as

$$\mathbf{Ax} = \mathbf{b}, \tag{2.7}$$

where \mathbf{x} is a column vector of length $(2N + 1)$, with elements

$$x_{2j-1} = \text{Re}(Q_j), \quad x_{2j} = \text{Im}(Q_j), \quad j = 1, 2, \dots, N, \tag{2.8a}$$

$$x_{2N+1} = \Omega, \tag{2.8b}$$

\mathbf{A} is an $M \times (2N + 1)$ matrix, with elements

$$a_{i,2j} + ia_{i,2j-1} = \log \left[\frac{z_i - z_j}{z_i - z_0} \right], \tag{2.9a}$$

$$a_{i,2N+1} = 1, \quad i = 1, 2, \dots, M, \quad j = 1, 2, 3, \dots, N, \tag{2.9b}$$

and \mathbf{b} is a column vector of length M , with elements

$$b_k = -y_k, \quad k = 1, 2, 3, \dots, M. \tag{2.10}$$

With $M \gg 2N + 1$, (2.7) is an over-determined system. A least-squares solution may be obtained by first premultiplying (2.7) by the transpose of \mathbf{A} . This leads to the normal

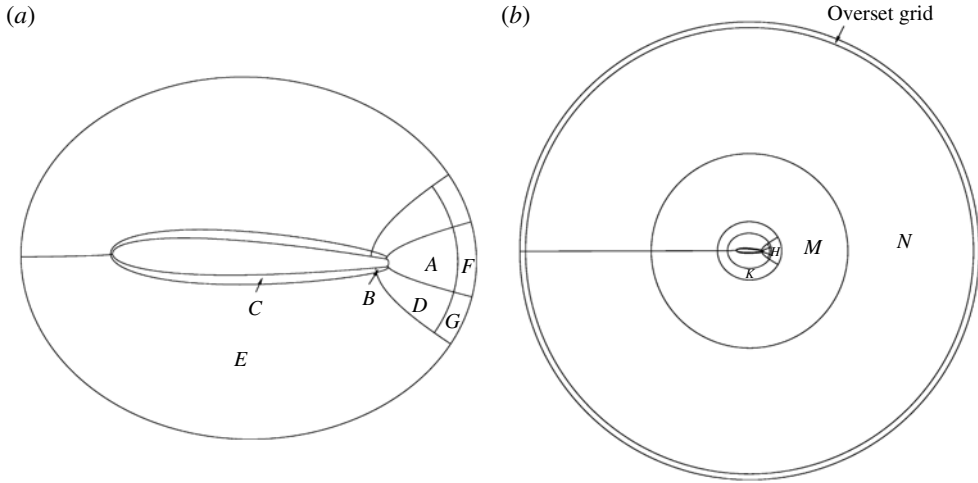


FIGURE 12. The various subdomains of a multi-size mesh in the physical space: (a) enlarged view near the aerofoil; (b) entire elliptic domain.

equation

$$\mathbf{A}^T \mathbf{A} \mathbf{x} = \mathbf{A}^T \mathbf{b}, \tag{2.11}$$

which can be easily solved by any standard matrix solver.

The second step in developing a body-fitted grid to the aerofoil is to take the mid-point of the slit in the $\xi-\eta$ plane as the centre of an elliptic coordinate system. Let the width of the slit be a and $\bar{\xi}$ be the x coordinate measured from the mid-point of the slit. The elliptic coordinates (μ, θ) are related to $(\bar{\xi}, \eta)$ by

$$\bar{\xi} = \frac{a}{2} \cosh \mu \cos \theta, \quad \eta = \frac{a}{2} \sinh \mu \sin \theta. \tag{2.12}$$

The elliptic coordinate system is shown in figure 11. The elliptic coordinate system is orthogonal. The curve $\mu = 0$ is the surface of the aerofoil in the physical plane. The boundary layer lies in the region $\mu < \Delta$ in the $\mu-\theta$ plane. The wake is in the region $-\Delta_1 < \theta < \Delta_2$, where Δ , Δ_1 and Δ_2 are small quantities. In the present simulations, these are the regions with the finest meshes.

The problem at hand is a multi-scale problem. The smallest length scale of the problem that needs to be resolved is in the viscous boundary layer and in the wake. In this work, a multi-size mesh is used in the time marching computation. Figure 12 shows the boundaries of the different mesh size blocks in the elliptical coordinates region of the computation domain. The mesh size increases by a factor of 2 as one crosses a mesh-size-change boundary going outwards from the aerofoil. For large μ , the elliptical coordinates become circular. At a radius of about eight chord widths, the computation switches from the $\mu-\theta$ coordinates to rectangular Cartesian coordinates in the physical plane, as shown in figure 13. The Cartesian mesh extends 10 chord lengths upstream and 30 chords downstream from the aerofoil. It is 10 chords wide on both top and bottom sides of the aerofoil. One reason for using such a large computational domain is to provide sufficient distance for the wake and shed vortices to develop fully and to decay before exiting the computational boundary. This minimizes the generation of disturbances that can reflect back into the computational domain. Another reason for using a wide and large domain is to lessen

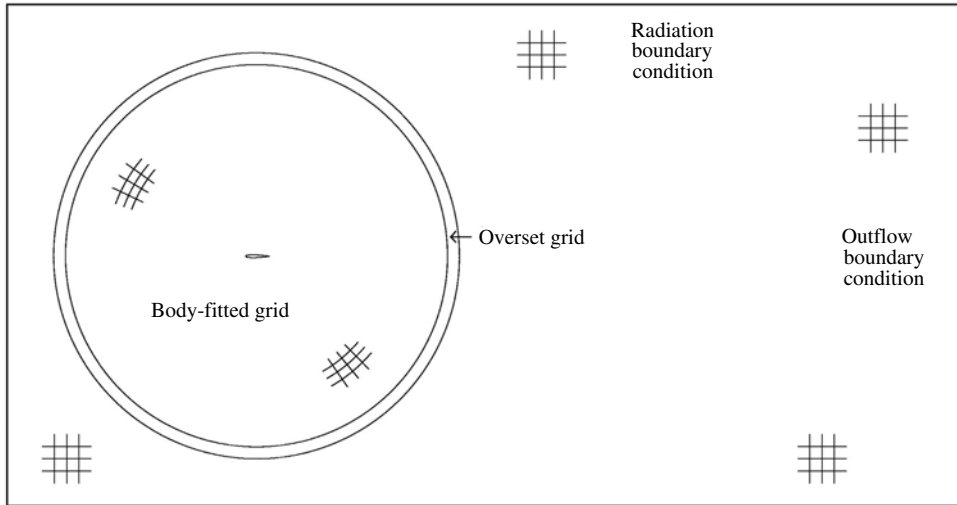


FIGURE 13. The entire computational domain showing the elliptic coordinates region, the Cartesian coordinates region and the overset grid.

the likelihood of the computational boundary becoming an anchor point of a feedback loop associated with the flow past the aerofoil.

The total number of mesh points used in the simulation is 1.84 million. In the boundary layer adjacent to the aerofoil, where the highest resolution is required, the mesh size Δ_n , in the direction normal to the aerofoil surface, is set equal to $\Delta_n/C = 4 \times 10^{-4}$. This gives 21 mesh points in the boundary layer at the trailing edge region at a Reynolds number of 5×10^5 . At a Reynolds number 2×10^5 , there are 33 mesh points in the boundary layer. Along the surface of the aerofoil, there are 2500 mesh spacings. This makes the aspect ratio of the mesh in the computational domain close to unity. In the near wake, the mesh size Δ_s in the flow direction (or θ direction) is $\Delta_s/C = 3.4 \times 10^{-4}$. Along the mesh line $\mu = \text{constant}$, the mesh has nearly the same resolution. This is to keep the mesh aspect ratio nearly equal to one. The reason for keeping the mesh aspect ratio nearly unity is because acoustic waves have no preferred direction of propagation.

2.3. Computational algorithm

For time marching computation in the elliptic coordinates region of the computational domain, (2.1)–(2.4) are first rewritten in the μ – θ coordinates. The derivatives are then discretized according to the seven-point stencil dispersion-relation-preserving (DRP) scheme of Tam & Webb (1993). At the mesh-size-change boundaries, the multi-size-mesh, multi-time-step DRP scheme of Tam & Kurbatskii (2003) is implemented. This scheme allows a smooth connection and transfer of the computed results using two different size meshes on the two sides of the boundary. Another important feature of this method is that it also allows a change in the size of the time step. This makes it possible to maintain numerical stability without being forced to use very small time steps in subdomains where the mesh size is large. This makes the computation efficient without loss of accuracy.

In the nearly circular region of the computation domain (see figure 13), the computation is carried out in the μ – θ plane. Outside this region, a rectangular mesh is used. The computation is performed in the x – y plane. At the overlapping boundary of these two regions, the overset grids method of Tam & Hu (2004) is used to transfer

data from one grid set to the other. The data transfer process is accomplished by the use of a 16-point optimized interpolation stencil. The interpolation process has a comparable accuracy to the time marching computation scheme.

Near the aerofoil surface, where backward difference stencils are used, artificial selective damping (see Tam, Webb & Dong 1993) is introduced to damp out spurious waves and grid-to-grid oscillations created by the presence of the wall (a discontinuity). In addition, general background artificial selective damping terms are added to all discretized governing equations. This ensures the removal of any residual spurious waves that might exist in the computational domain.

On the left, top and bottom boundaries of the computational domain shown in figure 13, the radiation boundary conditions developed by Tam & Webb (1993) are imposed. On the right side of the boundary, outflow boundary conditions given by them are enforced. On the aerofoil surface, the $u = v = 0$ no-slip boundary conditions are imposed. This, however, will create an over-determined system of equations if all the discretized governing equations are required to be satisfied at the boundary points. To avoid this problem, the two momentum equations of the Navier–Stokes equations are not enforced at the wall boundary points. The continuity and energy equations are, nevertheless, computed to provide the values of density ρ and pressure p at the aerofoil surface.

To start the computation, the variables are set equal to the values of the uniform flow, namely, $u = M$, $v = 0$, $\rho = 1$ and $p = 1/\gamma$. The solution is then time marched until it is periodic.

2.4. Grid refinement and code validation

To ensure that the numerical simulations in this study have adequate resolution, grid refinement has been implemented in two test cases. In this exercise, the mesh size in the elliptic coordinates region of the computational domain is reduced by half. The two test cases chosen are for aerofoil no. 3 at Reynolds number 2×10^5 and 4×10^5 . At Reynolds number 2×10^5 , the tone frequency found in the simulation remains the same at 1138 Hz. At Reynolds number 4×10^5 , the tone frequency computed using a coarse mesh is 3187 Hz. The tone frequency computed using a finer mesh is 3119 Hz. This represents a frequency change of 2%. On assuming that the difference is proportional to the Reynolds number of the simulation, we estimate that our results should be accurate to about 3% at the highest Reynolds number in the present study.

To provide assurance that the resolution of the present computation code is adequate, the time-averaged pressure coefficient $C_p = p / (\frac{1}{2} \rho U^2)$ at Reynolds number 4×10^5 is computed using our numerical simulation data for comparison with experiment. For this Reynolds number, Lee & Kang (2000) have earlier published a set of measured data. The measurements were carried out in a wind tunnel. The data set, corrected for wall blockage according to Lee & Kang, is shown in figure 14. Shown in this figure also are the measured C_p values from our numerical simulation. It is clear that there is good agreement between experimental and numerical simulation results.

To test the adequacy of the present computation code for acoustic computation, we compare the sound pressure level (SPL) of aerofoil tone measured in our numerical simulation at Reynolds number of 4×10^5 with the experimental measurements of Nash *et al.* (1999). The data of Nash *et al.* exhibit considerable scatter of the tone intensity. The data band has a deviation of ± 3.5 dB around the mean value. At a flow velocity of 58 m s^{-1} , our tone has an SPL of 95.3 dB. The mean value of the experimental data is 93.9 dB. Thus the SPL of our simulation result lies within the data scattering band of the experiment.

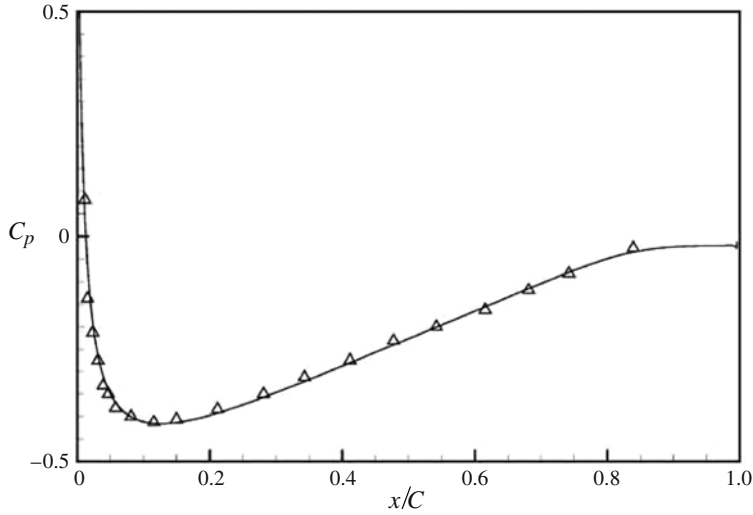


FIGURE 14. Comparison between computed pressure coefficient (full line) and experimental measurements (triangles) of Lee & Kang (2000).

It is our belief that the above tone SPL comparison with experiment, the C_p distribution comparison with experiment and the grid refinement study when taken together, indeed, provide confidence that the computer code developed in the present investigation has the resolution and accuracy for an in-depth aerofoil tone study.

3. Numerical results

In this section, the computed results of our numerical simulations are reported. We will first report the results of the flow field and then the acoustic results.

3.1. Flow field

At zero degree angle of attack, the computed boundary layer flow on the aerofoil remains attached almost to the trailing edge. The boundary layer flow is steady, while the flow in the wake is oscillatory. Figure 6 shows a plot of the computed instantaneous vorticity field around aerofoil no. 2 at a Reynolds number of 2×10^5 . The leading edge of the aerofoil is placed at $x = 0$. This is typical of all the cases investigated. The flow leaves the trailing edge of the aerofoil smoothly. There is no vortex shedding at the trailing edge, regardless of previous speculation (Paterson *et al.* 1973). The oscillations in the wake intensify in the downstream direction until it rolls up to form discrete vortices further downstream.

Figure 15 shows an instantaneous streamline pattern of the wake of aerofoil no. 2 at a Reynolds number of 4×10^5 . The wake oscillations are prominent in this figure. The wavelength of the oscillations appears to be fairly regular. This suggests that there is instability in the wake.

The mean velocity deficit profile in the wake resembles a Gaussian function. The half-width of the wake near the aerofoil trailing edge undergoes large variation in the flow direction. Figure 16 shows the variation of the half-width as a function of downstream distance for aerofoil no. 2 at a Reynolds number of 2×10^5 . The width of the wake begins to shrink right downstream of the aerofoil trailing edge until a minimum is reached at $b = b_{min}$. It grows rapidly further downstream, reaching a maximum before decreasing and attaining a nearly asymptotic value.

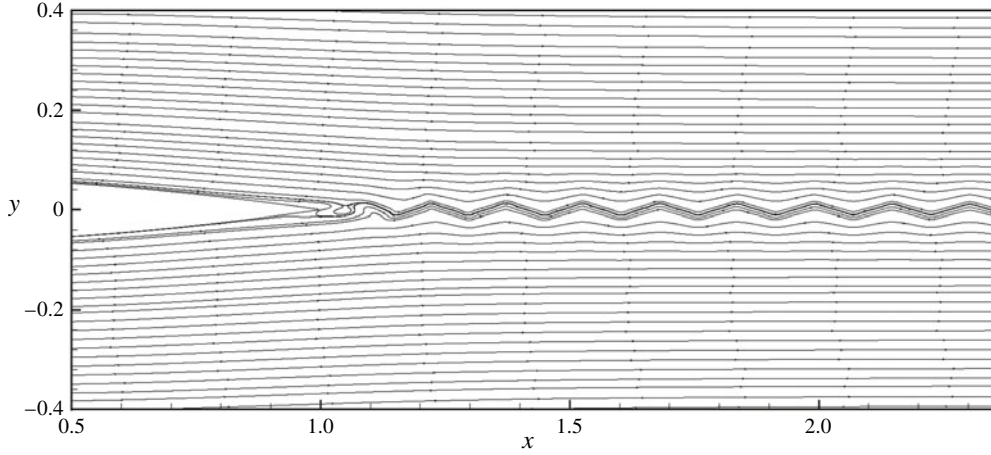


FIGURE 15. Instantaneous streamline pattern showing strong oscillations in the wake of the aerofoil: aerofoil no. 2, $Re = 4 \times 10^5$.

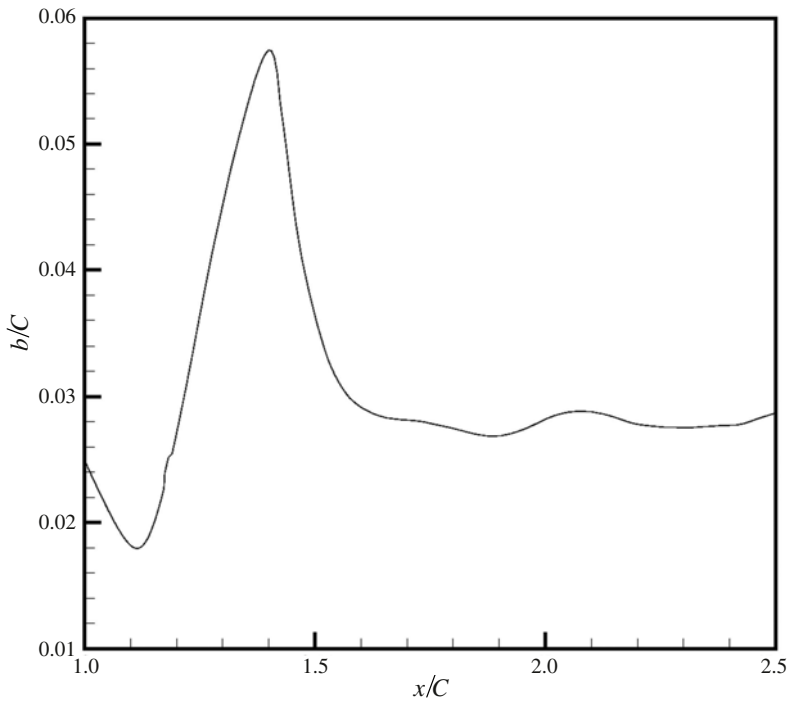


FIGURE 16. Spatial distribution of the half-width of the wake for Aerofoil no. 2 at $Re = 2 \times 10^5$.

The velocity deficit profiles of the wake exhibit self-similarity. Figure 17 shows a collapse of the velocity profiles at minimum half-width over a large range of Reynolds number. In this figure, the variable $(u - U_{min})/(U - U_{min})$ is plotted against y/b_{min} , where U_{min} is the minimum velocity of the mean flow profile and b is the half-width.

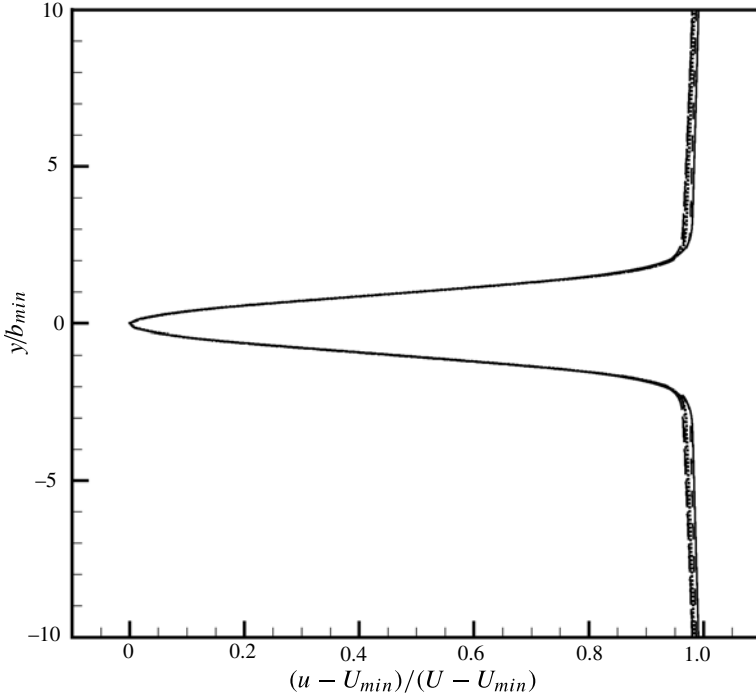


FIGURE 17. Similarity of velocity deficit profile at $b = b_{min}$ in the wake of aerofoil no. 2. Reynolds number varies from 2×10^5 to 5×10^5 at 0.5×10^5 interval.

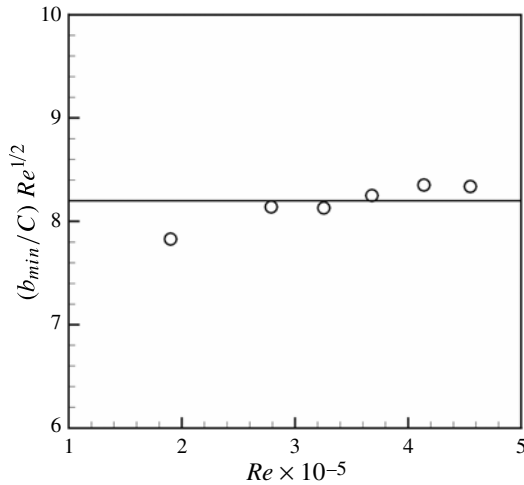


FIGURE 18. Relationship between b_{min} of the wake and Reynolds number (aerofoil no. 2).

In figure 17, data over Reynolds number from 2×10^5 to 5×10^5 at 0.5×10^5 interval are included. There is a nearly perfect match of the set of seven profiles.

The similarity property of the wake velocity profiles suggests the possibility of the existence of a simple correlation of the minimum half-width of the wake with flow Reynolds number (Re). Figure 18 shows a plot of $(b_{min}/C)Re^{1/2}$ against Re (C is the

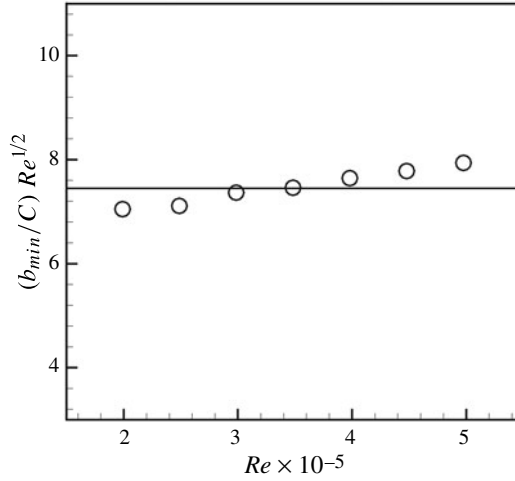


FIGURE 19. Relationship between b_{min} of the wake and Reynolds number (aerofoil no. 1).

chord width) for aerofoil no. 2. It is seen that the measured values of this quantity from the numerical simulations are nearly independent of Reynolds number over the entire range of Reynolds number of the present study. Thus the minimum half-width of the wake, b_{min} , of aerofoil no. 2 has the following form of Reynolds number dependence:

$$\frac{b_{min}}{C} Re^{1/2} \approx 8.2 \quad (\text{aerofoil no. 2}). \quad (3.1)$$

A similar analysis has been performed for aerofoil no. 1. Figure 19 shows that the quantity $(b_{min}/C)Re^{1/2}$ again is approximately a constant. In this case, the value b_{min} and Reynolds number are related by

$$\frac{b_{min}}{C} Re^{1/2} \approx 7.45 \quad (\text{aerofoil no. 1}). \quad (3.2)$$

There is a slight deviation of the computed data from a constant in figure 19. But the averaged error in using a constant is only about 3%.

3.2. Acoustics

In all the simulations we have performed for aerofoils nos. 1–3 (see table 1), only a single tone is detected. Figure 20 shows a typical aerofoil trailing edge tone that we have measured. This figure is the noise spectrum (bandwidth = 120 Hz) for aerofoil no. 1 at a Reynolds number of 4×10^5 . The measurement point is at (1.08, 0.5). Since there is only one single tone per computer simulation, it makes our finding the same as Nash *et al.* (1999).

Figure 21 shows the computed tone frequencies versus flow velocities for aerofoil no. 1 according to the results of our numerical simulations. This aerofoil has a 0.5% truncation. It is nearly a sharp trailing edge aerofoil. As shown in this figure, all the data points lie practically on a straight line parallel to the Paterson formula (the full line). The difference between our simulation results and the Paterson formula is very small. Based on what is shown in figure 21, we believe that our simulation, for all intents and purposes, reproduces the Paterson formula. We consider that the good agreement with the Paterson formula not only is proof of the validity of the

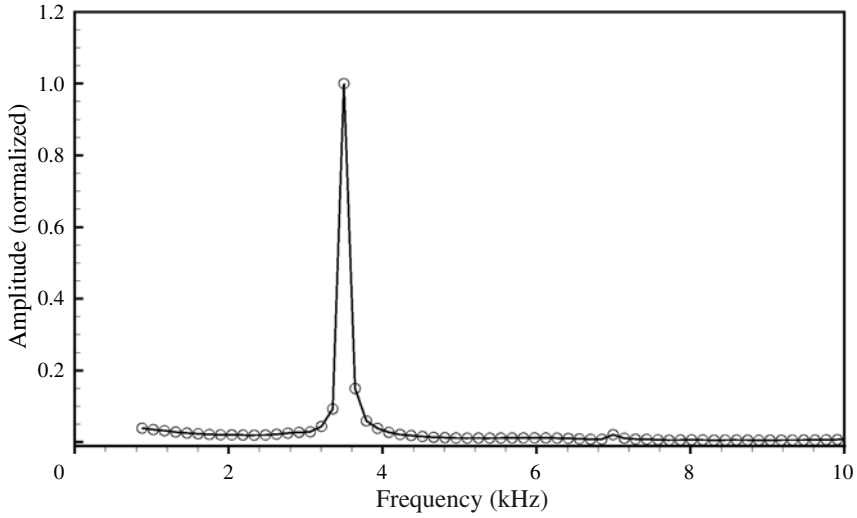


FIGURE 20. The measured noise spectrum for aerofoil no. 1 at $Re = 4 \times 10^5$.

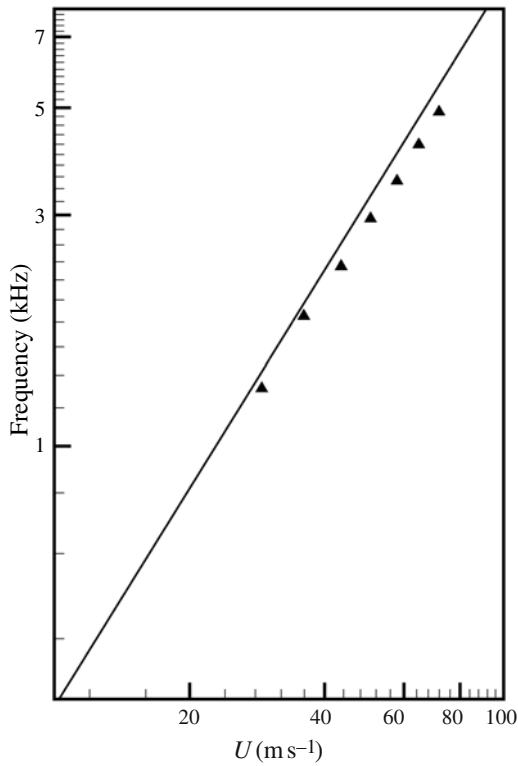


FIGURE 21. Measured tone frequencies at different flow velocities for aerofoil no. 1. The straight line is the Paterson formula.

simulations but also is an assurance that our simulations do contain the essential physics of aerofoil tone generation.

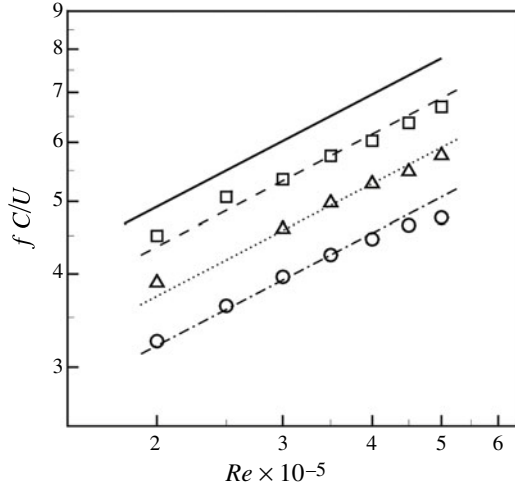


FIGURE 22. Dependence of tone Strouhal number on Reynolds number for aerofoils no. 1 (dashed), no. 2 (dotted) and no. 3 (dotted-dashed). The full line is the Paterson formula.

Aerofoil	Truncation (%)	Value of K
NACA0012	0	0.011 (Paterson formula)
no. 1	0.5	0.00973
no. 2	2.0	0.00835
no. 3	10.0	0.00717

TABLE 2. Values of proportionality constant K .

Figure 22 shows the variations of the Strouhal numbers of the computed tones for the three aerofoils under consideration with Reynolds number. The data for each aerofoil lies approximately on a straight line. The straight lines are parallel to each other and to the Paterson formula (shown as the full line in figure 22). All the four lines in figure 22 fit a single formula,

$$\frac{fC}{U} = KRe^{1/2}, \quad (3.3)$$

where K is a constant. Equation (3.3) may also be written in a form similar to the Paterson formula, i.e.

$$f = K \frac{U^{3/2}}{(Cv)^{1/2}}. \quad (3.4)$$

The values of the constant K for each aerofoil have been determined by best fitting to the simulation data. They are given in table 2.

Based on the computed results shown in figure 22, the effect of trailing edge thickness at a given Reynolds number is to lower the tone frequency. That is, the thicker the blunt trailing edge, the lower is the tone frequency. This dependence turns out to be similar to that of vortex shedding tones such as that emitted by a long circular cylinder in a uniform flow. For the long cylinder vortex shedding problem, the

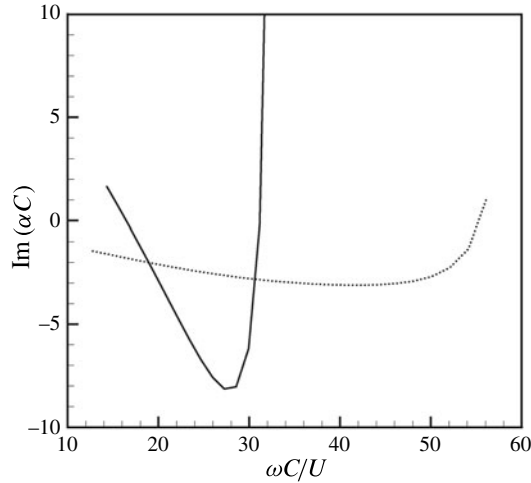


FIGURE 23. Comparison between the spatial growth rates of Kelvin–Helmholtz instability waves at the minimum half-width point in the wake (full curve) and at a point in the fully developed wake (dotted curve).

tone Strouhal number is approximately equal to 0.2, i.e.

$$\frac{fD}{U} \approx 0.2 \quad (3.5)$$

(D is the diameter). Therefore, the thicker the blunt object or trailing edge thickness, the lower is the tone frequency. However, it is to be noted that the physics and tone generation mechanisms are quite different.

4. Energy source of aerofoil tones

A number of investigators (see e.g. Tam 1974; Fink 1975; Arbey & Bataille 1983; Lowson *et al.* 1994; Nash *et al.* 1999; Desquesnes *et al.* 2007; Sandberg *et al.* 2007; Chong & Joseph 2009; Kingan & Pearse 2009) in the past have suggested that aerofoil tones are driven by instabilities of the boundary layer. Various computations of Tollmien–Schlichting type instabilities have been performed. The objective is to show that the frequency of the aerofoil tone is the same as that of the most amplified instability wave. An examination of the past computation reveals that the spatial growth rate of a Tollmien–Schlichting wave is very small. Only in the separated flow region is there a substantial growth rate. In the separated flow region, there is a rapid change in the mean flow profile. A non-parallel flow instability analysis would seem to be more appropriate in providing an accurate assessment of the instability wave characteristics.

In the present study, the NACA0012 aerofoil is set at zero degree angle of attack on purpose. At zero degree angle of attack, there is practically no flow separation on the aerofoil until almost the trailing edge. Thus the spatial growth rate of the Tollmien–Schlichting wave is much smaller than that of the Kelvin–Helmholtz instability in the wake of the aerofoil. It is known that the growth rate of a Kelvin–Helmholtz instability is inversely proportional to the half-width of the shear layer. In other words, a thin wake is more unstable than a thicker wake. That this is true is shown in figure 23. This figure shows the computed spatial growth rate (antisymmetric mode) over the distance of a chord for aerofoil no. 1 at different

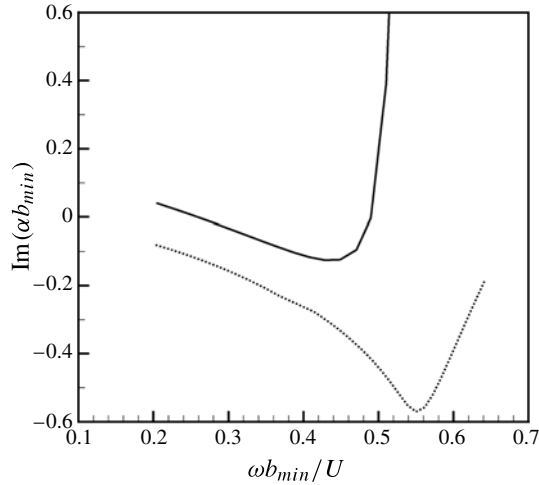


FIGURE 24. Comparison between the spatial growth rates of Kelvin–Helmholtz instability waves at the minimum half-width point using locally parallel (dotted curve) and non-parallel (full curve) instability theories. Aerofoil no. 2, $Re = 3 \times 10^5$.

instability wave frequencies. The computations are done using the non-parallel flow instability theory of Saric & Nayfeh (1975). The flow in the calculation has a Reynolds number of 3×10^5 . The solid curve is for the minimum half-width point of the wake at $x/C = 1.088$ measured from the leading edge of the aerofoil. The dotted curve is for a point in the developed wake region ($x/C = 1.556$). The maximum growth rate at the thinnest point of the wake is many times larger than that in the developed wake.

By performing an instability computation, it is easy to establish that the maximum growth rate occurs in the wake at the location where the wake half-width is minimum. It is our belief that, because the growth rate is very large, the instability initiated at this region is ultimately responsible for the generation of aerofoil tones. We will now provide the necessary computed instability results to support this hypothesis. Because of the rapid growth of the thickness of the wake at the minimum half-width location, we use the non-parallel flow instability wave theory of Saric & Nayfeh (1975) in all our computations. Their method is a perturbation method. The zeroth order is the locally parallel flow solution. A first-order correction, to account for the spreading of the mean flow, is then computed. The combined growth rate is taken as the non-parallel spatial growth rate. Figure 24 shows the difference between parallel and non-parallel spatial growth rates at the minimum wake half-width point for aerofoil no. 2 at a Reynolds number of 3×10^5 . It is straightforward to see from this figure that the non-parallel flow growth rate is smaller. Furthermore, the frequencies of the most amplified wave computed using parallel and non-parallel flow theories are quite different.

A comment on the appropriateness of the present instability wave analysis is in order. First of all, a linear theory is employed. This requires that the resulting motion is relatively small. Simulation data indicate that the maximum fluctuation velocity in the aerofoil wake is around 0.095 times the free stream velocity. Thus the dimensionless quadratic term of the perturbation velocity is about 1%. This may be small enough to ignore as a first approximation. Another important simplification in the present instability model is that the wake instability is assumed to be sufficiently

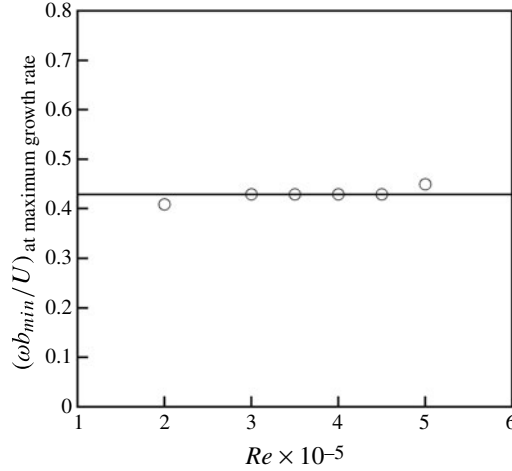


FIGURE 25. The angular frequency of the most amplified Kelvin–Helmholtz instability wave at the minimum half-width point of the wake as a function of Reynolds number. Aerofoil no. 2.

localized that a non-parallel localized analysis is adequate. One justification of this assumption, although not completely satisfactory, is that the instability is convective. That is, the instability wave has little upstream influence. In other words, there is little back-reaction of the Kelvin–Helmholtz instability on the aerofoil trailing edge flow. The influence is essentially one-way. That is, the flow around the aerofoil develops into a wake, which supports the instability. Implicitly, it is also assumed in the present model that the most dominant instability wave develops quickly and dominates (and prevents other subdominant waves from developing) the motion in the near wake.

Figure 25 shows the angular frequency of the Kelvin–Helmholtz instability wave with the highest amplification rate at the narrowest point of the wake of aerofoil no. 2 as a function of Reynolds number. When non-dimensionalized by minimum half-width b_{min} and free stream velocity U , the quantity $\omega b_{min}/U$ at maximum growth rate is nearly independent of Reynolds number. A good fit to the data is

$$\left(\frac{\omega b_{min}}{U} \right)_{\text{maximum growth}} \approx 0.43 \quad (\text{aerofoil no. 2}). \quad (4.1)$$

Now, for this aerofoil, b_{min} and Reynolds number are related by (3.1). By eliminating b_{min} from (3.1) and (4.1), it is found that

$$f = \frac{0.00835 U^{1.5}}{(Cv)^{1/2}}. \quad (4.2)$$

Equation (4.2) is exactly the same as (3.4) for aerofoil no. 2. The K value obtained directly from numerical simulations, displayed in table 2, is in agreement with that from instability consideration.

A similar non-parallel instability analysis for aerofoil no. 1 has also been carried out. Figure 26 shows the angular frequencies corresponding to that at maximum growth rate non-dimensionalized by b_{min} and U as a function of Reynolds number. An approximate relationship similar to (4.1) is

$$\frac{\omega b_{min}}{U} \approx 0.425 \quad (\text{aerofoil no. 1}). \quad (4.3)$$

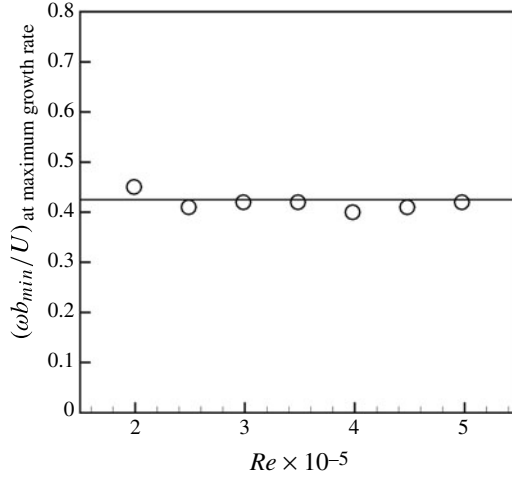


FIGURE 26. The angular frequency of the most amplified Kelvin–Helmholtz instability wave at the minimum half-width point of the wake as a function of Reynolds number. Aerofoil no. 1.

Thus, by eliminating b_{min} from (3.2) and (4.3), a tone frequency formula based on wake instability consideration for this aerofoil is

$$f = \frac{0.00910 U^{1.5}}{(Cv)^{1/2}}. \quad (4.4)$$

The proportionality constant in (4.4) differs only slightly from that found by DNS, as given in table 2. Figure 27 shows a direct comparison between the tone frequencies measured directly from numerical simulations (triangles) and the most unstable frequencies in the wake at minimum half-width (straight line). The agreement is quite good. We believe that the good agreements for aerofoil nos. 1 and 2 lend support to the validity of our proposition that the energy source of aerofoil tones at zero degree angle of attack is near-wake flow instability.

5. Sound generation processes

In the previous section, we have demonstrated that the energy source responsible for the generation of aerofoil tones is near-wake instability. These are antisymmetric instabilities. However, the flow is at low subsonic Mach number. It is known that low subsonic flow instabilities are, by themselves, not strong or efficient noise radiators. In this section, we report the results of our study of the space–time data of our numerical simulations. The objective of the study is to identify the tone generation processes. To facilitate this effort, we compute the fluctuating pressure field p' , defined by

$$p' = p - \bar{p}, \quad (5.1)$$

where \bar{p} is the time-averaged pressure. Positive p' indicates compression. Negative p' corresponds to rarefactions of the acoustic disturbances. Of special interest to us is the contour $p' = 0$. We will use this contour as an indicator of the acoustic wavefront. This is a good indicator outside the wake flow as the noise sources are localized in the near-wake and trailing edge region. We track the propagation of this contour from the aerofoil wake to the far field. The creation and spreading of the wavefront provides the clues needed for identifying the tone generation processes.

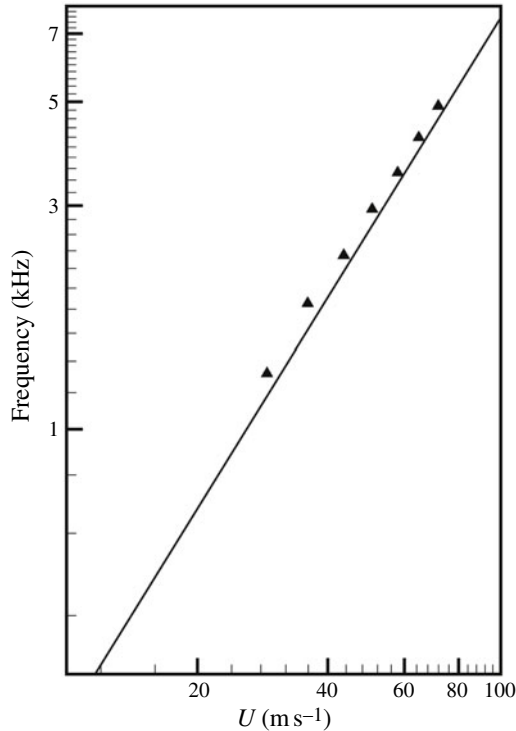


FIGURE 27. Comparison between DNS tone frequencies (triangles) and most amplified instability wave frequencies (straight line). Aerofoil no. 1.

Our study reveals that the tone generation processes are rather complex. There is a dominant mechanism involving the interaction between the near-wake oscillations driven by wake instability and the aerofoil trailing edge. However, there are also secondary mechanisms arising from adjustments of flow and vortices in the near wake. Details of these tone generation processes can be understood by following the motion of the wavefront contour $p' = 0$. Figure 28 illustrates the dominant tone generation process in space and time. Aerofoil no. 2 (2% truncation) at $Re = 4 \times 10^5$ is used in this simulation. Figure 28(a) may be regarded as the beginning of a tone generation cycle. The trailing edge of the aerofoil is shown on the left centre of the figure. The flow is from left to right. Thus the wake, defined by two $p' = 0$ contours, lies to the right of the aerofoil. The near wake is highly unstable. The instability causes the wake to oscillate, as can easily be seen in this figure. The wake is flanked by two rows of vortices in a staggered pattern. The spinning motion of the vortices creates a low-pressure region inside the vortices. Hence all the vortices are located in the $p' < 0$ regions. These regions are labelled (-). Regions with $p' > 0$ are labelled (+). Shown in figure 28(a) are wavefront contours of $p' = 0$. The near-wake instability is antisymmetric with respect to the x axis. This leads to an antisymmetric pressure field, as shown in all the panels in figure 28. The pressure field shown in figure 28(a) corresponds to the beginning of the downward motion of the wake in the region just downstream of the aerofoil trailing edge. Since the aerofoil is stationary, the downward movement of the near wake leads to the creation of a high-pressure region on the top side of the aerofoil trailing edge and a corresponding low-pressure region on the mirror image bottom side. This is shown as two small circular regions right

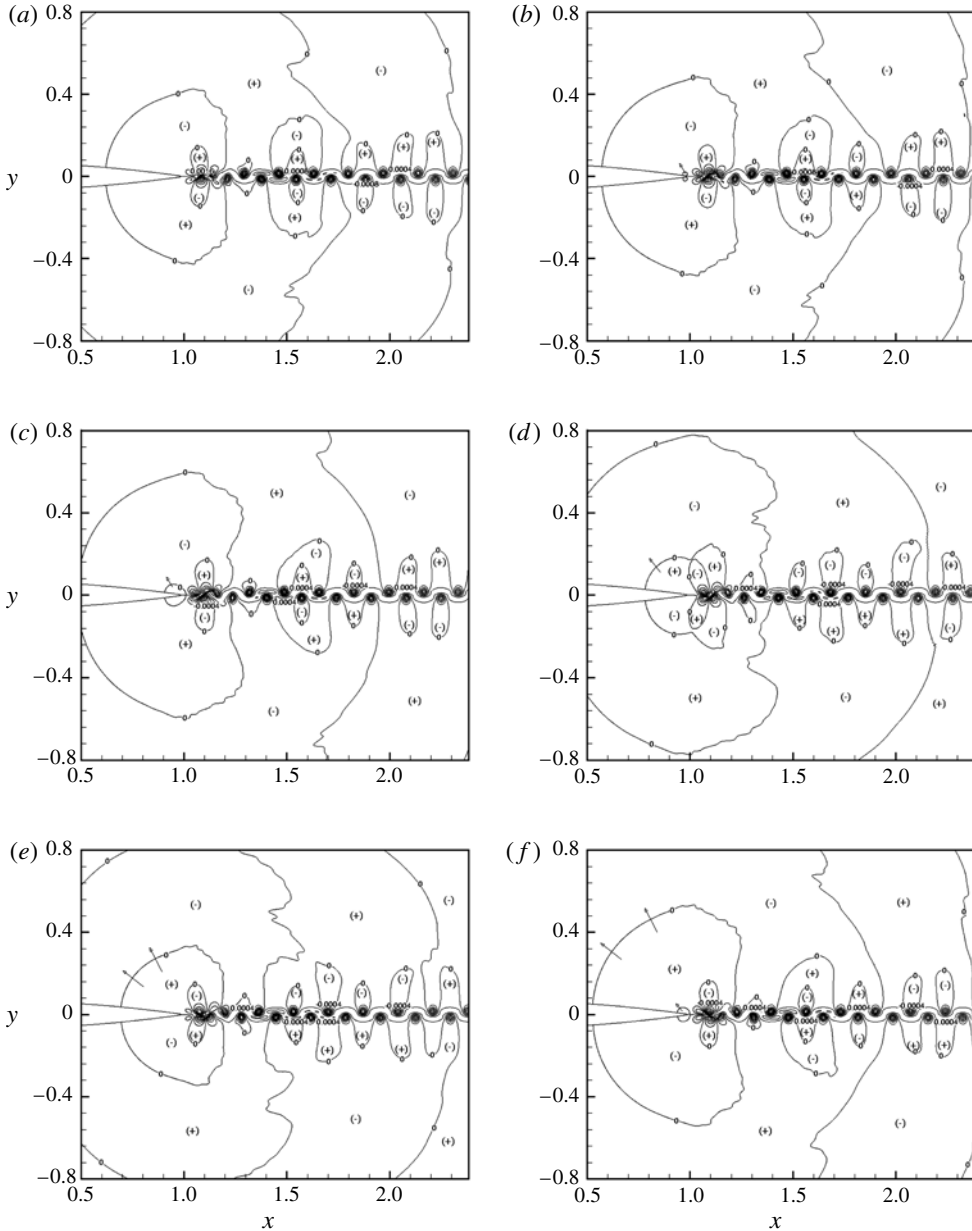


FIGURE 28. For caption see next page.

at the trailing edge of the aerofoil in figure 28(b). A small arrow is inserted there to indicate the direction of motion of the wavefront. The high- and low-pressure regions grow rapidly in time, as shown in figure 28(c-e). The time difference between figure 28(a) and (e) is nearly half a cycle. Hence, figure 28(e-h) repeat a similar sequence of wavefront motion but with positive and negative fluctuating pressure fields interchanged. Each wavefront contour in each half-cycle shows its creation at the trailing edge of the aerofoil, its expansion in space and time, and its propagation to the far field in all directions.

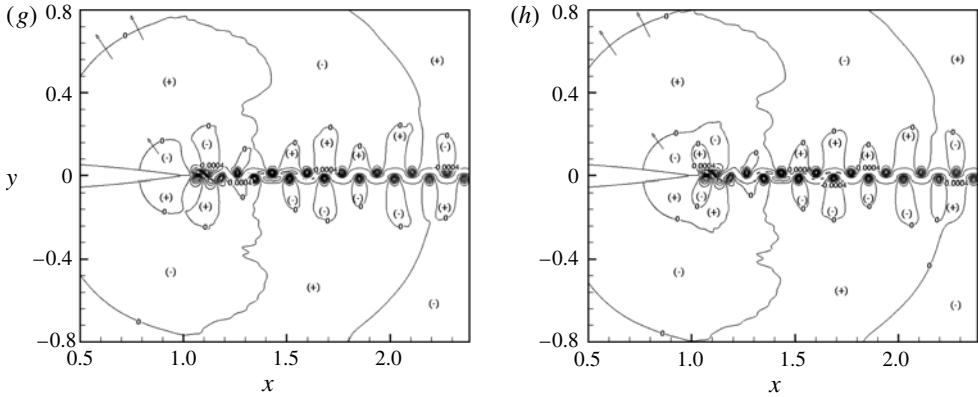


FIGURE 28. (cntd). Instantaneous positions of contour $p' = 0$ in the proximity of the near wake for aerofoil no. 2 at $Re = 4 \times 10^5$: (a) $t = 36.367T$; (b) $t = 36.402T$; (c) $t = 36.526T$; (d) $t = 36.69T$; (e) $t = 36.789T$; (f) $t = 36.974T$; (g) $t = 37.183T$; and (h) $t = 37.209T$; $T = \text{period}$.

The dominant tone generation process is observed in all the simulations that have been carried out. In some cases, other less dominant tone generation processes have been observed. These secondary processes may reinforce the primary process or may be important only in a certain direction of radiation. By and large, the secondary mechanisms are related to the adjustment of the flow from boundary layer type to free shear wake flow and also the realignment of the wake vortices from their creation to a vortex street.

Figure 29 illustrates a secondary tone generation process. Figure 29(a) may be taken as the distribution of the wavefront contours at the beginning of a cycle for aerofoil no. 2 at Reynolds number 2×10^5 . At the instant corresponding to figure 29(a), the near wake begins to move upwards. This creates a high-pressure region on the bottom side of the aerofoil trailing edge and at the same time a low-pressure region on the mirror image location on the top side. This is shown in figure 29(b). Figure 29(c) shows the expansion of the high- (bottom) and low-pressure (top) regions near the trailing edge. At the same time, this figure also shows the expansion of the next two loops; negative pressure regions in the top half of the figure and positive pressure regions in the lower half. The three negative pressure regions that have expanded are labelled as 1, 2 and 3 in this figure. The locations of loops 2 and 3 coincide with the region where the wake oscillations are strongest with largest lateral displacements (see figure 6). However, the wake has not rolled up to form vortices yet. Thus this secondary tone generation process does not involve the formation of discrete vortices. Figure 29(d–g) show the merging of the loops and the propagation of the wavefront to the far field. Therefore, for this case, the adjustment of the near-wake flow assists and contributes to the generation of the observed aerofoil tone.

For aerofoils with a sharp trailing edge especially when operating at the high end of the moderate Reynolds number range, the wake rolls up into discrete vortices very close to the trailing edge (see figure 30). In these cases, the formation of discrete vortices does contribute to the generation of aerofoil tones. This secondary tone generation process is illustrated in the motion of the wavefronts in figure 31. Figure 31(a) may be considered as the beginning of a tone generation cycle. To observe the secondary tone generation process, attention is directed to the shaded area of this figure. Figure 31(b) (at a later time) shows the expansion of the shaded region.

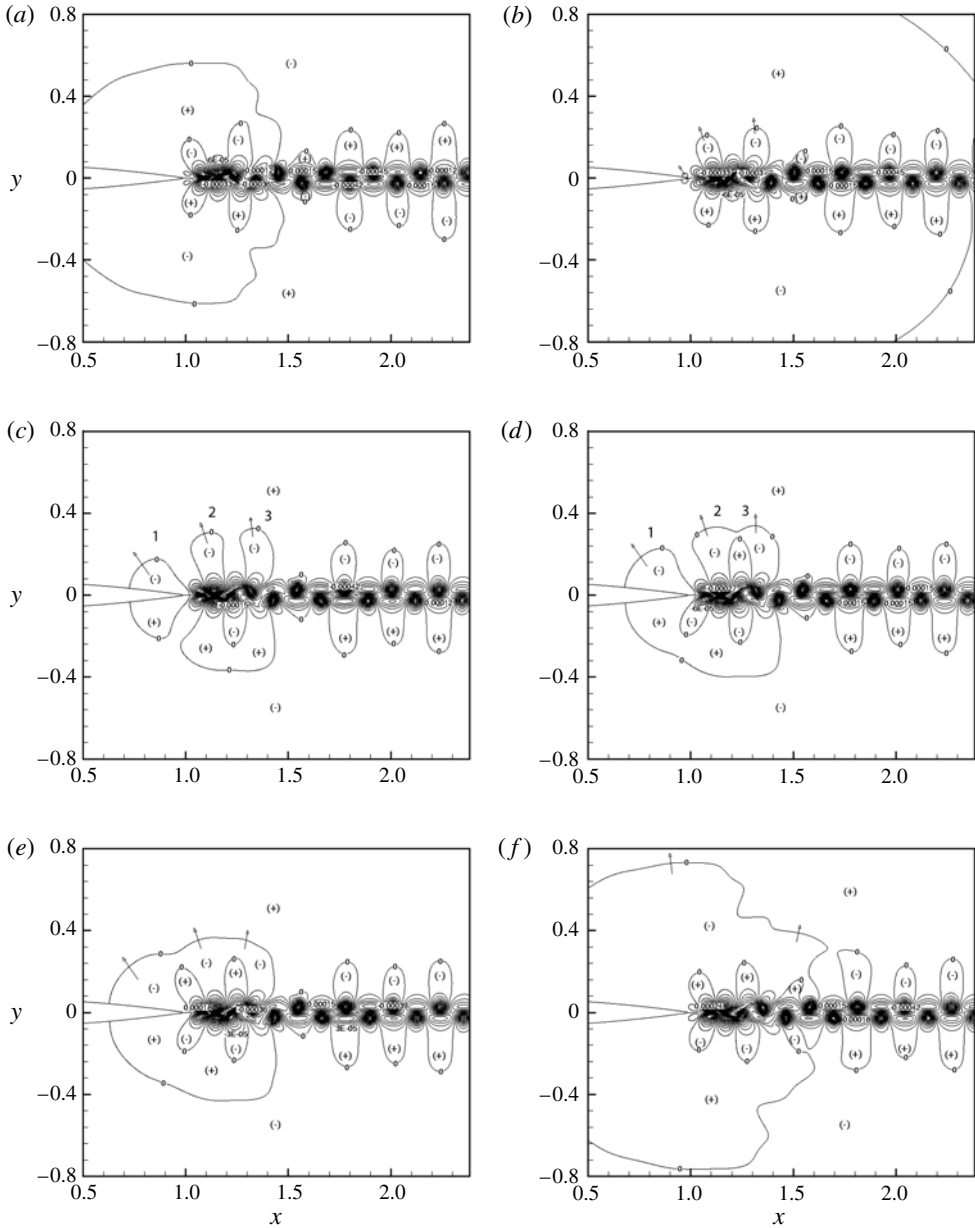


FIGURE 29. For caption see next page.

On comparing with figure 30, it is seen that the location of the expanded shaded region coincides with the beginning of the wake rolling up into isolated vortices. We are of the opinion that the formation of the vortices is what drives the expansion of the shaded region. Figure 31(c-h) track the continued spreading of the sound pulse after it is generated. It appears that the dominant tone generation mechanism due to the interaction of near-wake instability and the aerofoil trailing edge is responsible for radiating sound to the upstream and sideline directions. The secondary tone generation mechanism due to the formation of discrete vortices is responsible for radiating

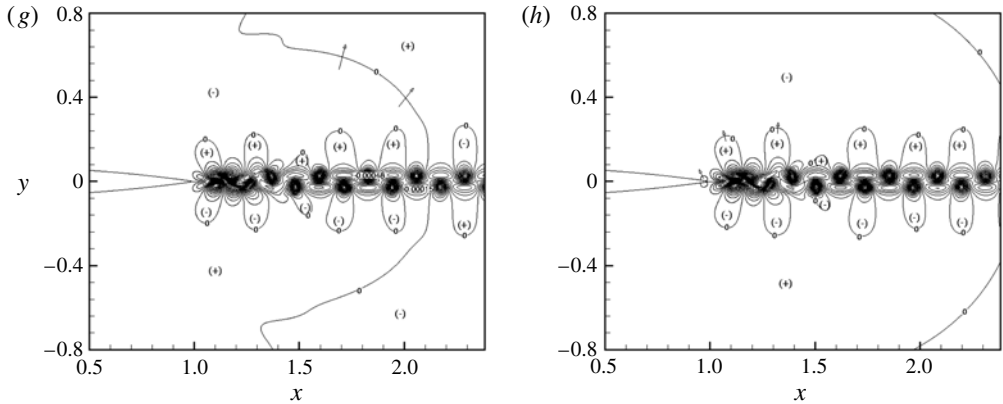


FIGURE 29. (cntd). Motion of wavefronts for aerofoil no. 2 at 2×10^5 Reynolds number illustrating a secondary tone generation process: (a) $t = 23.80T$; (b) $t = 24.02T$; (c) $t = 24.18T$; (d) $t = 24.201T$; (e) $t = 24.218T$; (f) $t = 24.35T$; (g) $t = 24.424T$; and (h) $t = 24.53T$; $T =$ period.

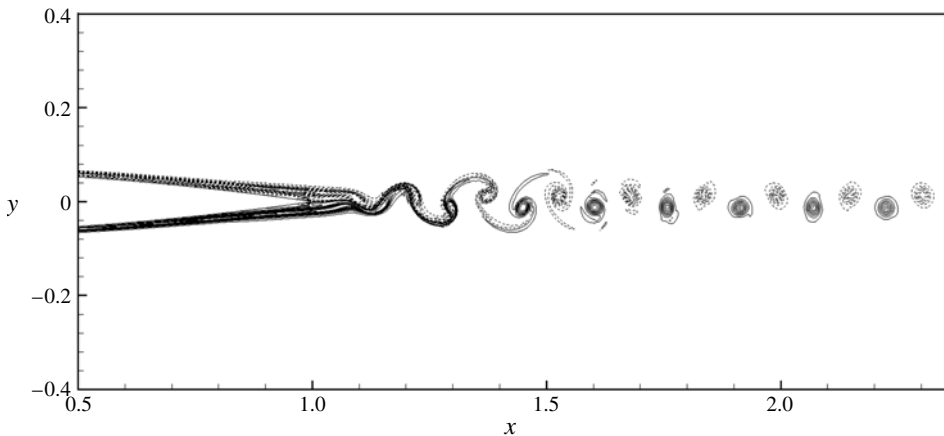


FIGURE 30. Vorticity contours showing the rolling up of the wake into discrete vortices near the sharp trailing edge of an aerofoil. Aerofoil no. 1 at $Re = 4 \times 10^5$.

sound to the downstream direction. The two mechanisms are perfectly coordinated and synchronized.

6. Summary and conclusions

In the past, there have been a number of experimental studies on aerofoil tones at moderate Reynolds number. Unfortunately, the measured results of the experiments differ substantially from each other. One of the objectives of the present investigation is to see if it is possible to provide a resolution to the disagreement by studying the tone generation phenomenon by a different method, namely, by DNS. An extremely attractive advantage of DNS is that there is no background wind tunnel (open or closed) noise or other facility-related noise. Also, by making the computational domain sufficiently large, it is possible to avoid acoustic feedback anchored to laboratory equipment or built-in hardware outside the wind tunnel, a possibility that

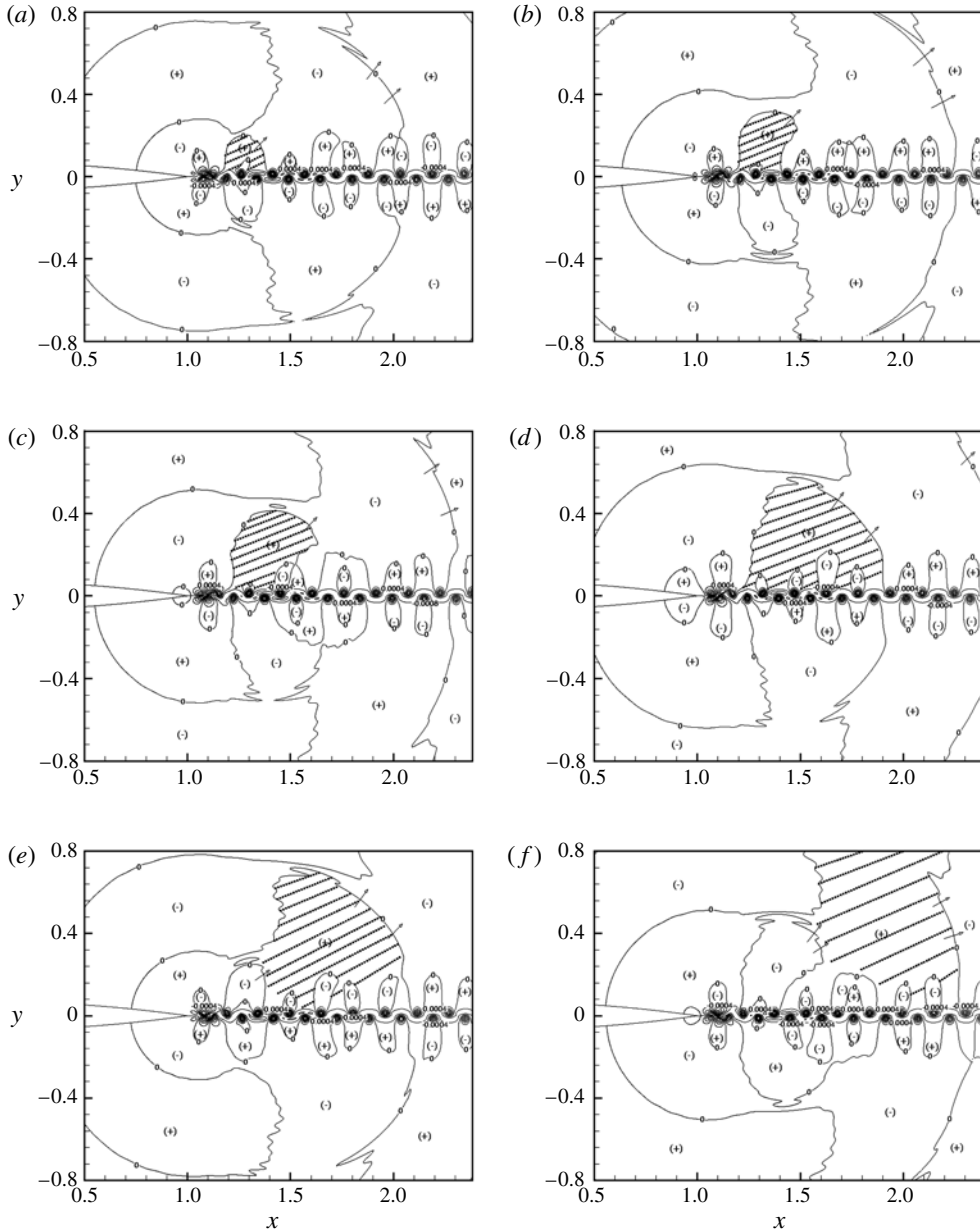


FIGURE 31. For caption see next page.

can happen in an experiment. In other words, DNS, when properly carried out, can simulate a truly isolated aerofoil in a uniform flow. In the present study, numerical results indicate that there is only one aerofoil tone for each simulation. This is true in all the simulations performed in the present investigation. Thus the present result is in agreement with the measurements of Nash *et al.* (1999). We agree with Nash *et al.* that the feedback tones observed by the other experiments are facility-related and are not genuine tones of isolated aerofoils.

In the present investigation, the tones of three NACA0012 aerofoils with different trailing edge thickness at zero degree angle of attack are studied. The reason for

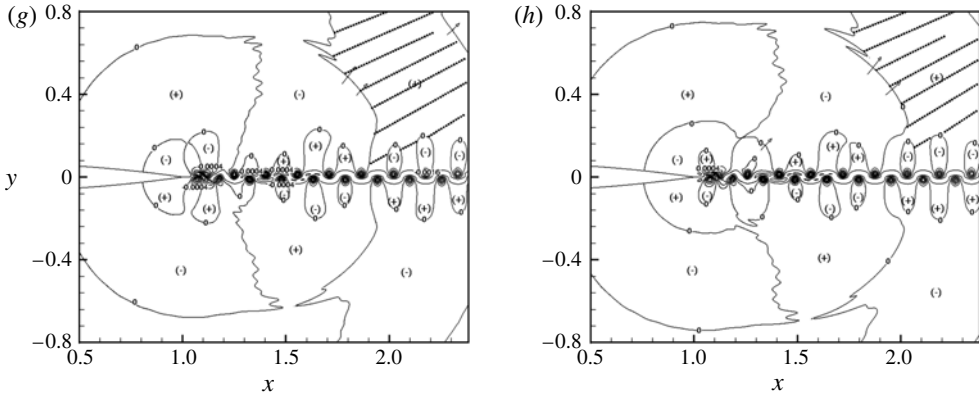


FIGURE 31. (cntd). A secondary tone generation mechanism due to the formation of discrete vortices in the wake illustrated by the motion of wavefront contours for aerofoil no. 1 at $Re = 4 \times 10^5$: (a) $t = 50.264T$; (b) $t = 50.41T$; (c) $t = 50.51T$; (d) $t = 50.643T$; (e) $t = 50.795T$; (f) $t = 51.002T$; (g) $t = 51.188T$; and (h) $t = 51.254T$; $T =$ period.

restricting the study to aerofoils at zero degree angle of attack is to keep the flow field around the aerofoil as simple as possible. At an angle of attack, flow separation may occur, creating a leading edge separation bubble or open separation. Under such a condition, tones may be generated by means other than the basic tone generation mechanism. For the aerofoil with the smallest trailing edge thickness, the computed tone frequency dependence on flow velocity is in good agreement with the Paterson formula. For an aerofoil with thicker trailing edges, the computed tone frequency versus flow velocity data are found to fit a formula identical in form to the Paterson formula but with a different proportionality constant. This set of DNS data suggest that an aerofoil with a thicker trailing edge would have lower tone frequency at the same flow velocity. This finding is new. It is consistent with intuitive expectation.

The search for the energy source responsible for the emission of aerofoil tones is a part of the present investigation. Past experience with wake and boundary layer instabilities leads to the proposal that it is the near-wake Kelvin–Helmholtz instability that provides the energy for acoustic radiation. Since the thinner the wake, the larger is the instability amplification rate, it follows that the frequency of the most amplified instability wave, including non-parallel flow effect, where the wake is thinnest should dictate the tone frequency. By following this idea, it is straightforward to derive an aerofoil tone frequency formula through instability analysis. The formula derived is found to be in good agreement with the tone frequencies measured from DNS data over the entire range of moderate Reynolds number. The good agreement lends support to the proposed near-wake instability mechanism. This also provides a general method to predict aerofoil tone frequency through instability theory.

The processes by which near-wake instability generates strong tones are investigated by analysing the space–time data obtained by DNS. By using the zero-fluctuation pressure contour ($p' = 0$) as an indicator of wavefront, it is identified that the principal tone generation mechanism is the interaction between the near-wake oscillations driven by flow instability and the trailing edge of the aerofoil. The wake oscillations cause the formation of transient high- and low-pressure regions on the opposite sides of the aerofoil trailing edge. The creation and expansion of the high- and low-pressure regions lead to sound radiation. In addition to the principal mechanism, there are secondary mechanisms. The secondary mechanisms arise from the adjustment of

near-wake flow and the formation of discrete vortices in the wake. We would like to point out again that the present investigation is restricted to aerofoils at zero degree angle of attack. In this flow configuration, the boundary layer flow is attached to the aerofoil almost to the trailing edge. For aerofoils at a finite angle of attack, a separation bubble as well as open separation may form on the suction side of the aerofoil. Under these circumstances, other noise and tone generation mechanisms become possible and might even be dominant. To determine these new mechanisms is, without doubt, a challenging endeavour. Such effort is, however, beyond the scope of the present investigation.

Acknowledgements

The authors wish to acknowledge the support of the Florida Center for Advanced Aero-Propulsion (FCAAP) under FSU Project no. 024809.

REFERENCES

- ARBEY, H. & BATAILLE, J. 1983 Noise generated by airfoil profiles placed in a uniform laminar flow. *J. Fluid Mech.* **134**, 33–47.
- BERS, A. 1975 Linear waves and instabilities. In *Physique des Plasmas* (ed. C. DeWitt & J. Peyraud). pp. 117–215. Gordon and Breach.
- BRIGGS, R. J. 1964 *Electron-Stream Interaction with Plasmas*. MIT Press.
- CHONG, T. P. & JOSEPH, P. 2009 An experimental study of tonal noise mechanism of laminar airfoils. *AIAA Paper* 2009-3345.
- DESQUESNES, G., TERRACOL, M. & SAGAUT, P. 2007 Numerical investigation of the tone noise mechanism over laminar airfoils. *J. Fluid Mech.* **591**, 155–182.
- FINK, M. R. 1975 Prediction of airfoil tone frequencies. *J. Aircraft* **12**, 118–120.
- JONES, L. E. & SANDBERG, R. D. 2010 Numerical investigation of tonal airfoil self-noise generated by an acoustic feedback-loop. *AIAA Paper* 2010-3701.
- KINGAN, M. J. & PEARSE, J. R. 2009 Laminar boundary layer instability noise produced by an aerofoil. *J. Sound Vib.* **322**, 808–828.
- KOCH, W. 1985 Local instability characteristics and frequency determination of self-excited wake flows. *J. Sound Vib.* **99**, 53–83.
- KUROTAKI, T., SUMI, T., ATOBE, T. & HIYAMA, J. 2008 Numerical simulation around NACA0015 with tonal noise generation. *AIAA Paper* 2008-0672.
- LEE, H. & KANG, S. H. 2000 Flow characteristics of transitional boundary layers on an airfoil in wakes. *Trans. ASME: J. Fluids Engng* **122**, 522–532.
- LOWSON, M. V., FIDES, S. P. & NASH, E. C. 1994 Laminar boundary layer acoustic instabilities. *AIAA Paper* 94-0358.
- MCALPINE, A., NASH, E. C. & LOWSON, M. V. 1999 On the generation of discrete frequency tones by the flow around an airfoil. *J. Sound Vib.* **222**, 753–779.
- NAKANO, T., FUJISAWA, N. & LEE, S. 2006 Measurement of tonal-noise characteristics and periodic flow structure around NACA0018 airfoil. *Exp. Fluids* **40**, 482–490.
- NASH, E. C., LOWSON, M. V. & MCALPINE, A. 1999 Boundary-layer instability noise on airfoils. *J. Fluid Mech.* **382**, 27–61.
- OERLEMANS, S. 2003 Wind tunnel aeroacoustic tests of six airfoils for use on small wind turbines. NREL SR-500-34470. National Aerospace Laboratory, Emmeloord, The Netherlands.
- PATERSON, R. W., VOGT, P. G., FINK, M. R. & MUNCH, C. L. 1973 Vortex noise of isolated airfoils. *J. Aircraft* **10**, 296–302.
- SANDBERG, R. D., JONES, L. E., SANDHAM, N. D. & JOSEPH, P. F. 2009 Direct numerical simulations of tonal noise generated by laminar flow past airfoils. *J. Sound Vib.* **320**, 838–858.
- SANDBERG, R. D., SANDHAM, N. D. & JOSEPH, P. F. 2007 Direct numerical simulations of trailing-edge noise generated by boundary-layer instabilities. *J. Sound Vib.* **304**, 677–690.

- SARIC, W. S. & NAYFEH, A. H. 1975 Nonparallel stability of boundary layer flows. *Phys. Fluids* **18**, 945–950.
- SHARLAND, I. J. 1964 Sources of noise in axial flow fans. *J. Sound Vib.* **1**, 302–322.
- STOLZ, S., ADAMS, N. A. & KLEISER, L. 2001 An approximate deconvolution model for large-eddy simulation with application to incompressible wall bounded flows. *Phys. Fluids* **13**, 997–1015.
- TAM, C. K. W. 1974 Discrete tones of isolated airfoils. *J. Acoust. Soc. Am.* **55**, 1173–1177.
- TAM, C. K. W. & HU, F. Q. 1989 On the three families of instability waves of high speed jets. *J. Fluid Mech.* **201**, 447–483.
- TAM, C. K. W. & HU, F. Q. 2004 An optimized multi-dimensional interpolation scheme for computational aeroacoustics applications using overset grids. *AIAA Paper* 2004-2812.
- TAM, C. K. W. & KURBATSKII, K. A. 2003 Multi-size-mesh multi-time-step dispersion-relation-preserving scheme for multiple scales aeroacoustics problems. *Intl J. Comput. Fluid Dyn.* **17**, 119–132.
- TAM, C. K. W. & WEBB, J. C. 1993 Dispersion-relation-preserving scheme for computational acoustics. *J. Comput. Phys.* **107**, 262–281.
- TAM, C. K. W., WEBB, J. C. & DONG, A. 1993 A study of the short wave component in computational acoustics. *J. Comput. Acoust.* **1**, 1–30.